

TURBULENT CONVECTION IN STELLAR INTERIORS. III. MEAN-FIELD ANALYSIS AND STRATIFICATION EFFECTS

MAXIME VIALLET^{1,2}, CASEY MEAKIN^{3,4,5}, DAVID ARNETT⁴, AND MIROSLAV MOCÁK³

¹ Physics and Astronomy, University of Exeter, Stocker Road, Exeter, EX4 4QL, UK

² Max-Planck-Institut für Astrophysik, Karl Schwarzschild Strasse 1, Garching, D-85741, Germany

³ Theoretical Division, Los Alamos National Laboratory, Los Alamos, NM 87545, USA

⁴ Steward Observatory, University of Arizona, Tucson, AZ 85721, USA

⁵ New Mexico Consortium, Los Alamos, NM 87544, USA

Received 2012 December 25; accepted 2013 March 11; published 2013 April 29

ABSTRACT

We present three-dimensional implicit large eddy simulations of the turbulent convection in the envelope of a $5 M_{\odot}$ red giant star and in the oxygen-burning shell of a $23 M_{\odot}$ supernova progenitor. The numerical models are analyzed in the framework of one-dimensional Reynolds-Averaged Navier–Stokes equations. The effects of pressure fluctuations are more important in the red giant model, owing to larger stratification of the convective zone. We show how this impacts different terms in the mean-field equations. We clarify the driving sources of kinetic energy, and show that the rate of turbulent dissipation is comparable to the convective luminosity. Although our flows have low Mach numbers and are nearly adiabatic, our analysis is general and can be applied to photospheric convection as well. The robustness of our analysis of turbulent convection is supported by the insensitivity of the mean-field balances to linear mesh resolution. We find robust results for the turbulent convection zone and the stable layers in the oxygen-burning shell model, and robust results everywhere in the red giant model, but the mean fields are not well converged in the narrow boundary regions (which contain steep gradients) in the oxygen-burning shell model. This last result illustrates the importance of unresolved physics at the convective boundary, which governs the mixing there.

Key words: convection – hydrodynamics – stars: evolution – stars: interiors – turbulence

Online-only material: color figures

1. INTRODUCTION

Since the original publication of the mixing length theory (MLT) by Böhm-Vitense (1958), much effort has been devoted to the improvement of the theory (Gough 1977; Stellingwerf 1982; Xiong 1986; Kuhfuss 1986; Canuto & Mazzitelli 1991; Canuto 1992; Gehmeyr & Winkler 1992; Wuchterl & Feuchtinger 1998; Deng et al. 2006). Nevertheless, MLT still remains the standard choice in most state-of-the-art stellar evolution codes.

With the wealth of data coming from asteroseismology missions (*CoRoT*, *Kepler*), and expected from future observatories (*Gaia*, *JWST*), a new generation of stellar models is needed. The modeling of solar-like oscillations requires reliable models for the Reynolds stresses (Belkacem et al. 2006; Samadi et al. 2012). The interaction between convection and pulsations, which sets the location of the red edge of the instability strip, needs a better time-dependent theory of turbulent convection (Buchler & Kolláth 2000). In the deep interior, additional mixing is required at convective boundaries across the Hertzsprung–Russell diagram, above convective cores (Maeder 1975; Matračka et al. 1982; Schroder et al. 1997), and below convective envelopes (Herwig 2000; Pace et al. 2012). Lacking a physically consistent description of this process (Renzini 1987), extra-mixing is currently included in stellar evolution codes with ad hoc parameterizations, so that predictive powers are hampered by the use of free parameters. Next generation stellar evolution models should rely on a consistent description of convective boundary mixing, together with the effect of internal waves induced by turbulence.

The road to a satisfying theory of turbulent convection is difficult. Stellar convection is highly turbulent, with Reynolds and Rayleigh numbers having “astronomical” values ($Re > 10^{10}$,

$Ra > 10^{20}$). The ongoing development of computational physics allows numerical modeling of turbulent systems having an increasing number of degrees of freedom, but at present no direct simulation of the problem is possible. Nevertheless, physical insight provided by computer simulations is invaluable in improving our understanding of stellar hydrodynamical processes. The path starting from large three-dimensional (3D) data sets and ending with a recipe simple enough to be implemented in stellar evolution codes is not straightforward. Ideally, a common framework should be used both for the analysis of multi-dimensional data and for stellar evolution calculations, strengthening the underlying connection and making the projection from 3D to one-dimensional (1D) easier. Reynolds-Averaged Navier–Stokes (RANS) equations are a promising framework for this. Much effort has been already devoted to RANS in the context of stellar hydrodynamics, see, e.g., Canuto (1997, 2011), Xiong et al. (1997), Canuto & Dubovikov (1998), Deng et al. (2006), and references therein. We adopt the same methodology.

A theory of turbulent convection should have a broad range of applicability: ideally to every type of star at all stages of evolution. Therefore, it is important to identify fundamental properties of the physical process and to understand what changes with different stellar conditions. This is an ambitious project, which we start by considering two very different astrophysical cases: the convection in the envelope of a $5 M_{\odot}$ red giant star, and the convection in the oxygen-burning shell of a $23 M_{\odot}$ supernova progenitor.

The paper is organized as follows: in Section 2 we present an overview of our stellar models and numerical tools. In Section 3, we develop a set of 1D RANS equations as a framework to analyze our data. Results are presented in Section 4. In Section 5, we summarize our findings and conclude the paper.

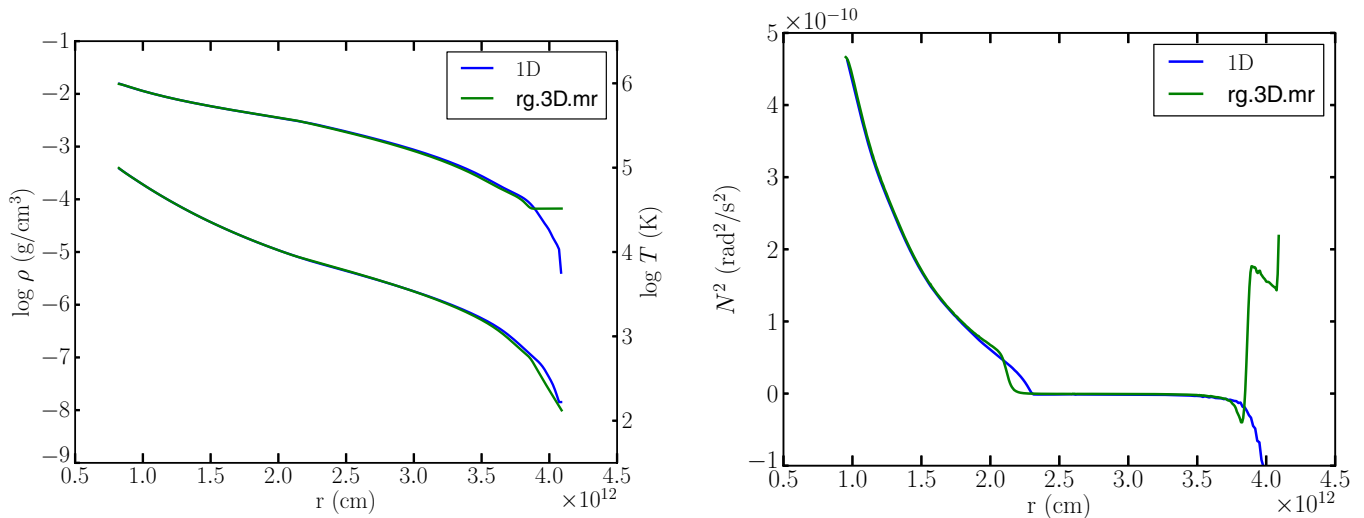


Figure 1. Overview of the simulated region in the red giant model. Left panel: density (bottom curves) and temperature (top curves) stratification in the initial (1D) and 3D model rg.3D.mr. Right panel: squared Brunt-Väisälä frequency in the initial (1D) and 3D model rg.3D.mr. (A color version of this figure is available in the online journal.)

2. STELLAR MODELS AND NUMERICAL METHODS

In this section we describe the stellar models and the hydrodynamic codes, and summarize the properties of the 3D models.

2.1. Red Giant Models

The red giant model was presented in Viallet et al. (2011). The initial 1D structure was constructed by integrating the stellar structure equations with the following input parameters: $M = 5 M_{\odot}$, $T_{\text{eff}} = 4500$ K, $\log(L/L_{\odot}) = 3.1$. In terms of stellar evolution phase, such a model would correspond to a $5 M_{\odot}$ star at the end of central He burning, finishing its blue loop and evolving toward lower T_{eff} and away from the red edge of the Cepheid Instability Strip (see Alibert et al. 1999, their Figure 1 and Table 6). The stellar structure code is described in Baraffe & El Eid (1991). It uses MLT (with $\alpha = 1.7$) to treat convection, and the extent of the convective region is based on the Schwarzschild criterion. The structure was integrated from the photosphere down to 20% of the stellar radius, stopping to avoid the nuclear burning region. This initial stratification is used as an input model for the multi-dimensional hydrodynamic code. The initial stellar structure is shown in Figure 1. The left panel shows the temperature and density stratifications. The model is characterized by a total density stratification $\log(\rho_{\text{bottom}}/\rho_{\text{top}}) \sim 4.4$. The total pressure stratification (not shown) is $\log(p_{\text{bottom}}/p_{\text{top}}) \sim 6.2$, or equivalently ~ 14.3 pressure scale-heights. The right panel shows the radial profile of N^2 , the Brunt-Väisälä frequency squared. The convective region extends down to $r \sim 2.3 \times 10^{12}$ cm, nearly half of the star in radius. The surface layers are characterized by a strong superadiabatic stratification.

As in Viallet et al. (2011), we use a proxy for the surface layers. The surface layers are numerically difficult to handle: the decrease in the pressure scale-height yields small scale convective eddies which are difficult to resolve when a single grid is used (see discussion in Viallet et al. 2011). To mimic surface cooling, we apply a Newtonian cooling term in the last 5% of the star:

$$q = \rho c_v \frac{T - T_0}{\tau} f(r), \quad (1)$$

where $f(r)$ is a spatially varying function that is equal to 1 above a given radius r_c with a smooth transition to zero, τ is the cooling timescale and T_0 is the forcing temperature. We use the same parameters as in Viallet et al. (2011): $r_c = 0.95 R_*$, $T_0 = 32,750$ K, and $\tau = 10^4$ s. About 4.5 pressure scale-heights of the initial 1D model are absorbed into the Newtonian cooling region.

We solve the equations describing the evolution of density, momentum, and total energy for a single fluid, taking into account gravity, radiative diffusion, and surface cooling:

$$\frac{\partial}{\partial t} \rho = -\nabla \cdot (\rho \mathbf{u}), \quad (2)$$

$$\frac{\partial}{\partial t} \rho \mathbf{u} = -\nabla \cdot (\rho \mathbf{u} \otimes \mathbf{u}) - \nabla p + \rho \mathbf{g}, \quad (3)$$

$$\frac{\partial}{\partial t} \rho \epsilon_t = -\nabla \cdot (\rho \epsilon_t \mathbf{u} + p \mathbf{u}) + \rho \mathbf{u} \cdot \mathbf{g} + \nabla \cdot (\chi \nabla T) - q, \quad (4)$$

where ρ is the density, \mathbf{u} the velocity, $\epsilon_t = \epsilon_i + \epsilon_k$ the specific total energy (ϵ_i is the specific internal energy and ϵ_k the specific kinetic energy), p the gas pressure, T the temperature, \mathbf{g} the gravitational acceleration, and χ the thermal conductivity. For photons, the thermal conductivity is given by

$$\chi = \frac{16\sigma T^3}{3\kappa\rho}, \quad (5)$$

where κ is the Rosseland mean opacity, and σ the Stefan-Boltzmann constant.

The 3D simulations were performed with the MUSIC code, as described in Viallet et al. (2011, 2013). The spatial method is based on a finite volume discretization of a spherical wedge (“box in a star” approach). The method is based on staggered velocity components, and has been extended to 3D for this work. The time-marching scheme used for the models presented in this paper is based on the Minimum Residual Approximate Implicit Scheme from Botchev et al. (1999). The MUSIC code is optimized to run on parallel computers and it uses domain-decomposition to distribute the computation over the

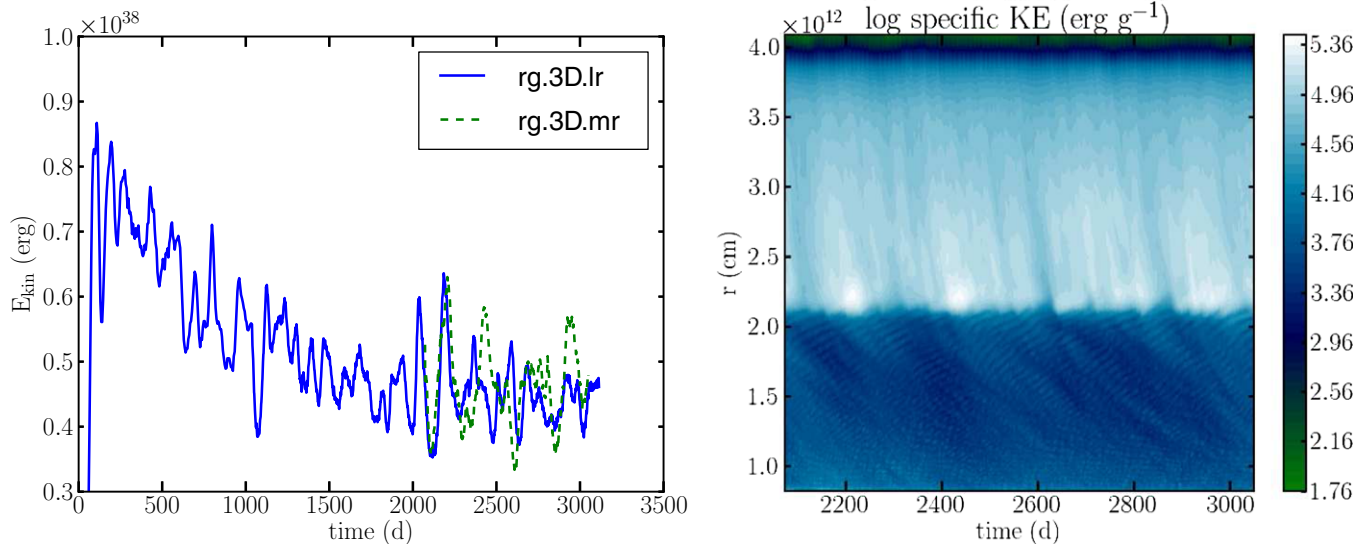


Figure 2. Left panel: evolution of the total kinetic energy in the red giant models. Right panel: space-time diagram of the specific kinetic energy in model rg.3D.mr. (A color version of this figure is available in the online journal.)

computational nodes. The Message Passing Interface (MPI) is used to handle communications of boundary data. We use periodic boundary conditions in horizontal directions, and non-penetrative stress-free conditions at the bottom and top of the domain. As the nuclear burning region is not included in the computational domain, a radiative flux corresponding to the stellar luminosity is imposed at the inner boundary.

We do not model viscosity explicitly in the equations. The expected value of the molecular viscosity in stellar interiors implies huge Reynolds numbers (larger than 10^{10}). It is therefore impossible to model all scales of the flow, from the stellar scale down to the dissipation scale, on current generation of computers. We adopt the Implicit Large Eddy Simulation paradigm (ILES; Grinstein et al. 2007) and solve the inviscid equations to model the turbulent flow. The underlying motivation of ILES is that monotonic, finite-volume-based methods have physical properties of the Navier–Stokes equations “built-in” within the numerics (unlike spectral and finite difference methods). The conservation properties of finite volumes schemes and the monotonicity preserving property enforce correct physical behavior at the grid scale. As a result, the loss of information that takes place at the grid scale mimics turbulent dissipation (see Section 4.1.2).

Models with two different resolutions were computed: model rg.3D.lr with a 216×128^2 resolution, and model rg.3D.mr with a 432×256^2 resolution. The main properties of these models are summarized in Table 1. We use an opening angle of $45^\circ \times 45^\circ$. Model rg.3D.lr was evolved for 3100 days of model time (for $\sim 3.6 \times 10^4$ CPU hours on 512 cores) and model rg.3D.mr was evolved for 1050 days of model time (for $\sim 2 \times 10^5$ CPU hours on 2048 cores), starting from the solution at $t = 2000$ days of model rg.3D.lr. The computations were performed on the IBM iDataPlex supercomputer “Hydra” at the Rechenzentrum Garching, and on the SGI Altix ICE 8200 supercomputer “Zen” at the University of Exeter. At the beginning of the computation, the Newtonian cooling term modifies the top layers and this triggers the convective instability. Downdrafts form and sink. They break up rapidly due to hydrodynamical instabilities, and the flow becomes turbulent. The left panel of Figure 2 shows the evolution of the total kinetic energy (KE) in the domain. The initial rise of the total KE is strong, followed

Table 1
Summary of the Red Giant Simulations

Parameter	rg.3D.lr	rg.3D.mr
Grid zoning	216×128^2	432×256^2
$r_{\text{in}}, r_{\text{out}}$ (10^{12} cm)	0.82, 4.09	0.82, 4.09
$\Delta\theta, \Delta\phi$	$45^\circ, 45^\circ$	$45^\circ, 45^\circ$
CZ stratification (H_p)	7.8	7.8
$t_{\text{av}}(\Delta t_{\text{av}})$ (days)	2650(800)	2650(800)
v_{rms} (10^5 cm s $^{-1}$)	2.27	2.34
τ_{conv} (days)	204	198
L_\star (10^{36} erg s $^{-1}$)	4.9	4.9
L_d (10^{36} erg s $^{-1}$)	7.33	7.39
l_d (10^{11} cm)	7.0	7.7
τ_d (days)	18	19
Pe	4900	5200

Notes. v_{rms} : global rms velocity, τ_{conv} : convective turnover timescale, L_\star : luminosity of the stellar model, L_d : rate of kinetic energy dissipation, l_d : dissipation length-scale, τ_d : dissipation timescale, Pe: Péclet number.

by a slow decay toward a quasi steady state. The left panel of Figure 1 shows the temperature and density stratifications obtained in the 3D model when a quasi-steady state is reached. The effect of the Newtonian cooling is to drive an isothermal region at the top. The right panel of Figure 1 shows the profile of N^2 in the 3D model. The most striking feature is the modification of the radial profile of N^2 , which shows a much steeper slope at the bottom boundary of the convective zone (CZ) in the 3D model than in the initial 1D model. This is an evidence for overshooting, and will be discussed in Section 4.6. In the 3D model, the density stratification is $\log(\rho_{\text{bottom}}/\rho_{\text{top}}) \sim 2.3$ in the CZ. The pressure stratification is $\log(p_{\text{bottom}}/p_{\text{top}}) \sim 3.4$ in the CZ, or equivalently ~ 7.8 pressure scale-heights. Clarifying the influence of such a large stratification on the properties of the turbulent convection is an important focus of this work. Figure 3 shows the radial profiles of the rms values of the density, temperature, and pressure fluctuations, normalized by their mean values. In the bulk of the convective region, all fluctuations have the same relative order of magnitude.

Computer animations and snapshots of the models illustrate the strong asymmetry of the flow, with the presence of plumes

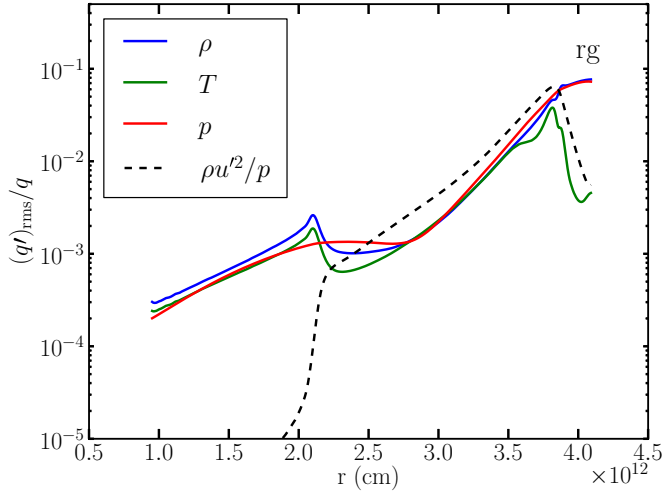


Figure 3. Radial profiles of the rms fluctuations of density, temperature, and pressure (continuous lines) in model rg.3D.mr. The black dashed line shows $\rho u^2/p$ for comparison (see discussion in Section 4.3).

(A color version of this figure is available in the online journal.)

triggered by cooling at the surface that sink in the CZ within much slower upflowing material. This is due to the degree of stratification, as emphasized by previous 3D simulations (Stein & Nordlund 1989; Cattaneo et al. 1991; Brummell et al. 1996, 2002; Porter & Woodward 2000). These plumes form a “network” of downflows in strong interaction, and from time to time plumes coalesce to form a strong downdraft which sinks through the whole stratification. The right panel of Figure 2 shows a space-time diagram of the specific KE, which shows the imprint of these sporadic events. The left panel of Figure 4 is a snapshot of the flow, as seen in the magnitude of the vorticity vector field $\omega = \nabla \times \mathbf{u}$ and emphasizes the prominence of small scale structures, characteristic of 3D turbulence. The right panel

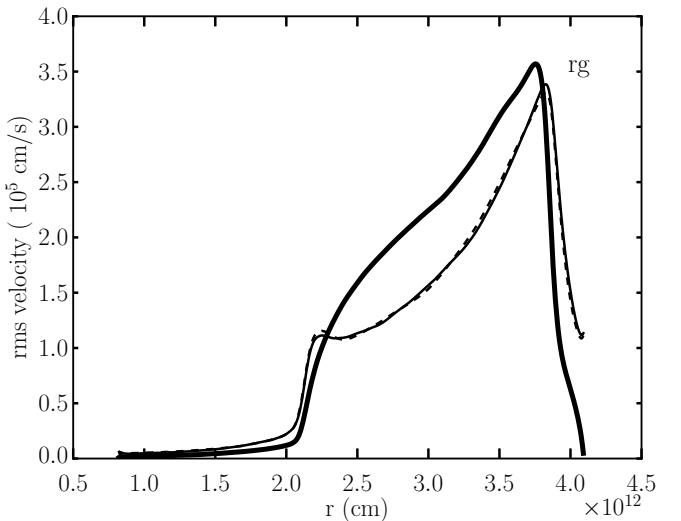
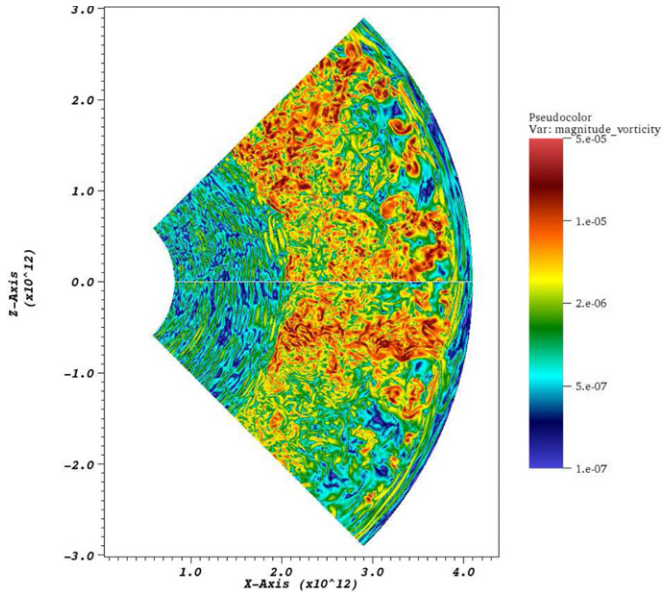


Figure 4. Left panel: snapshots of the computational domain for model rg.3D.mr. The magnitude of the vorticity $||\omega||$ is shown (two perpendicular cuts in the vertical direction were taken and are plotted together). Right panel: radial profiles of rms velocity components for model rg.3D.mr : u_r (thick solid line), u_θ (thin solid line), and u_ϕ (thin dashed line).

(A color version of this figure is available in the online journal.)

of Figure 4 shows the rms values of the velocity components u_r , u_θ , u_ϕ . The tangential and azimuthal components are roughly equal as the angular directions are homogeneous. Including rotation and/or magnetic fields would break this symmetry. The corresponding Mach number goes from ~ 0.1 at the top of the CZ to ~ 0.01 at the bottom. As in Arnett et al. (2009), we define a global rms velocity such as

$$\frac{1}{2} M_{CZ} v_{\text{rms}}^2 = E_{k,CZ}, \quad (6)$$

where M_{CZ} and $E_{k,CZ}$ are the total mass and KE in the CZ, respectively. The CZ is taken as the region between $r_{\text{in}} = 2 \times 10^{12}$ cm and $r_{\text{out}} = 4 \times 10^{12}$ cm, but we have checked that results are not too sensitive to these values. We find $v_{\text{rms}} = 2.34 \times 10^5$ cm s $^{-1}$ for model rg.3D.mr. We define the convective turn-over timescale as

$$\tau_{\text{conv}} = 2 \frac{l_{CZ}}{v_{\text{rms}}}, \quad (7)$$

which yields $\tau_{\text{conv}} = 198$ days for model rg.3D.mr.

Finally, Figure 4 and the right panel of Figure 2 hint at the presence of g-modes in the underlying radiative zone. The modes are excited at the convective boundary layer. In this paper, we will focus on the dynamics in the convective region, and leave the study of wave excitation and dynamics for future work.

2.2. Oxygen-burning Shell Models

We simulate the turbulent flow in a convective oxygen burning shell using as initial conditions a $23 M_\odot$ stellar model of solar composition that was previously evolved with the TYCHO stellar evolution code (Arnett et al. 2009) up to a point where oxygen, neon, carbon, helium, and hydrogen are burning in concentric shells about a silicon-sulfur rich core. Additional details can be found in Meakin & Arnett (2006, 2007). As in

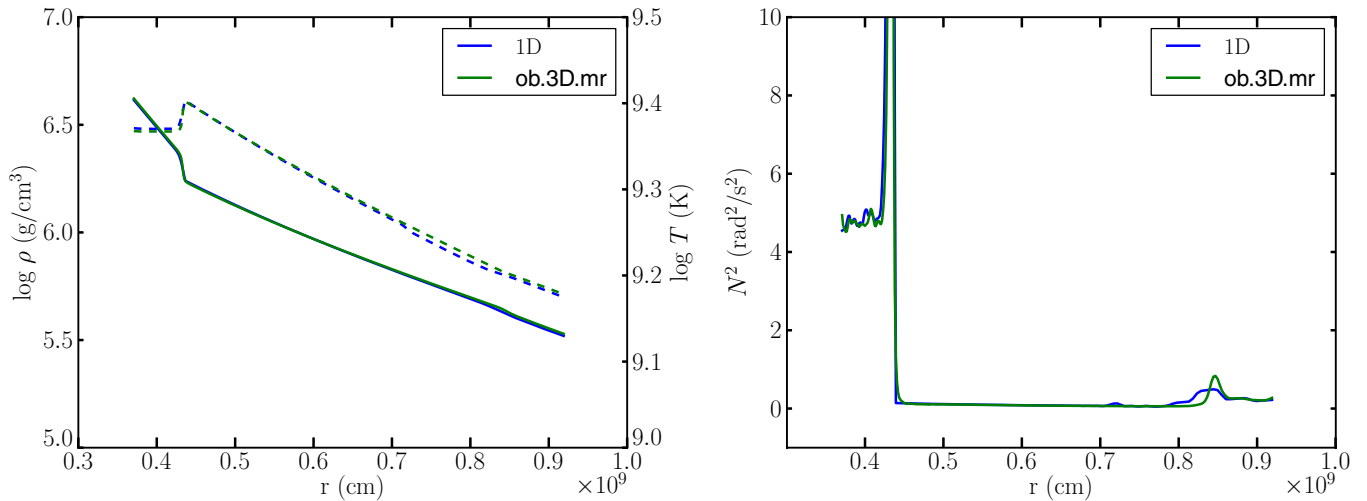


Figure 5. Overview of the simulated region in the oxygen-burning shell model for the initial model (1D) and for the 3D model ob.3D.mr. Left panel: density (continuous line) and temperature (dashed line) stratification. Right panel: squared Brunt–Väisälä frequency.

(A color version of this figure is available in the online journal.)

Meakin & Arnett (2007), we study only the oxygen burning convection zone and its stably stratified bounding layers.

Reactive-hydrodynamic evolution was simulated with the PROMPI code (Meakin & Arnett 2007), a distributed memory adaptation of the PROMETHEUS code (Fryxell et al. 1989), an Eulerian implementation of the piecewise parabolic method (PPM) hydrodynamics scheme (Colella & Woodward 1984) extended to treat realistic equations of state (Colella & Glaz 1985), multi-species advection, and a general nuclear reaction network. The setup for these simulations are nearly identical to that described in Meakin & Arnett (2007), including the 25 species followed to track nuclear evolution, and differ only in terms of resolution and domain size. As with the MUSIC code, PROMPI solves the inviscid equations, and we rely on the ILES paradigm to model sub-grid scale dissipation. The major differences between the two is that PROMPI is multi-fluid, includes nuclear burning, and that radiative diffusion is negligible in this context (Arnett 1996). Figure 5 shows the initial density and temperature stratifications (left panel), and the initial profile of N^2 (right panel). The latter is characterized by a narrow peak at the bottom boundary of the CZ, due to the sharp composition gradient that characterizes the boundary of the nuclear burning region. We refer the reader to Meakin & Arnett (2007) for similar figures as those shown earlier for the red giant model.

As with the red giant models, the oxygen shell burning models studied in this paper use a $45^\circ \times 45^\circ$ opening angle. Models with three different spatial resolutions were computed: model ob.3D.lr with 192×128^2 zones, model ob.3D.mr with 384×256^2 zones, and model ob.3D.hr with 768×512^2 zones. The main properties of these models are summarized in Table 2. Models ob.3D.lr and ob.3D.mr are used for comparison with the red giant models, whereas model ob.3D.hr is used to further assess the numerical convergence of our results with resolution (see Section 4.7). All of the oxygen burning models were computed on the University of Tennessee’s Kraken Cray XT5. Model ob.3D.lr was evolved for approximately 600 s of model time (on 768 cores for $\sim 5 \times 10^4$ CPU hours). Model ob.3D.mr was evolved for approximately 280 s of model time (on 12,288 cores for $\sim 3.5 \times 10^5$ CPU hours) starting from the solution at $t = 300$ s of model ob.3D.lr. Model ob.3D.hr was evolved

Table 2
Summary of the Oxygen Burning Simulations

Parameter	ob.3D.lr	ob.3D.mr	ob.3D.hr
Grid zoning	192×128^2	384×256^2	768×512^2
$r_{\text{in}}, r_{\text{out}}$ (10^9 cm)	0.3, 1.0	0.3, 1.0	0.3, 1.0
$\Delta\theta, \Delta\phi$	$45^\circ, 45^\circ$	$45^\circ, 45^\circ$	$45^\circ, 45^\circ$
CZ stratification (H_p)	2	2	2
$t_{\text{av}}(\Delta t_{\text{av}})$ (s)	494(230)	494(230)	429(165)
v_{rms} (10^6 cm s $^{-1}$)	9.2	9.57	9.2
τ_{conv} (s)	96	92	96
L_{nuc} (10^{46} erg s $^{-1}$)	2.69	2.63	2.47
L_d (10^{46} erg s $^{-1}$)	0.30	0.29	0.30
l_d (10^8 cm)	4.9	5.5	4.7
τ_d (s)	26	29	26

Notes. v_{rms} : global rms velocity, τ_{conv} : convective turnover timescale, L_{nuc} : total energy released by nuclear burning, L_d : rate of kinetic energy dissipation, l_d : dissipation length-scale, τ_d : dissipation timescale.

for approximately 200 s of model time (on 24,576 cores for $\sim 4 \times 10^6$ CPU hours) starting from the solution at $t = 310$ s of model ob.3D.mr.

At the beginning of the computation, the convective instability is triggered by a band of random, small amplitude density perturbations ($\rho'/\rho \sim 10^{-4}$) imposed within the convection zone. The flow rapidly becomes turbulent as it fills the convectively unstable region. The early transient evolution of the models is characterized by a strong penetration of the flow in the top stable region. After roughly 300 s, a quasi steady-state obtains with a slow evolution resulting from a net heating due to the imbalance between nuclear burning and neutrino cooling (a common feature of neutrino-cooled stages of stellar evolution which results in growth of the convective region). As a result, global characteristics of the model (e.g., total nuclear burning, total KE, etc.) increase slowly with time. The nuclear evolution timescale for this phase is roughly 5×10^3 s. The convective region is characterized by a density stratification $\rho_{\text{bottom}}/\rho_{\text{top}} \sim 6$, and a pressure stratification $p_{\text{bottom}}/p_{\text{top}} \sim 7.5$ or two pressure scale-heights. The global rms velocity and turnover timescale are computed as for the red giant (see previous section), and shown in Table 2. Figure 6 shows the radial profiles of the rms

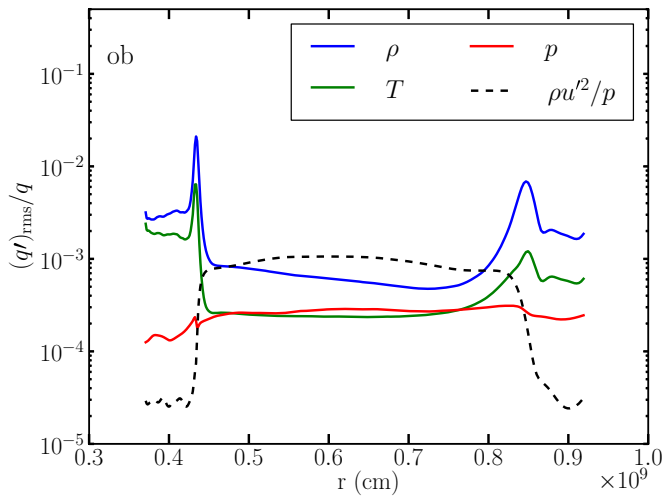


Figure 6. Same as Figure 3, but for the oxygen-burning shell model ob.3D.mr. (A color version of this figure is available in the online journal.)

values of the density, temperature, and pressure fluctuations, normalized by their averaged values. The largest values in the relative magnitude of the fluctuations occur at the boundaries, and are of the order of a percent.

3. HORIZONTALLY-AVERAGED MEAN-FIELD EQUATIONS

Using the RANS methodology, in this section we develop a framework of mean-field equations which are consistent with spherical geometry. A similar approach has been applied to the KE equation; see Hurlburt et al. (1986, 1994) and Meakin & Arnett (2007). We show here how this can be extended, as the KE is only one of the several mean-field equations that can be derived from the hydrodynamical equations. Although we refer to our equations as “RANS” equations, we actually introduce the effect of viscosity only through the KE dissipation rate ϵ_d (units: $\text{erg s}^{-1} \text{g}^{-1}$). In the large Reynolds number regime, the viscous dissipation is the dominant contribution of viscosity in the mean-field equations. This is the so-called “dissipation anomaly” characteristic of 3D turbulence; see the discussion in Section 4.7. Other terms, such as the viscous flux of KE, are neglected.

To obtain our set of 1D equations, we introduce two types of averaging: (1) statistical averaging, denoted by an overbar; (2) horizontal averaging, denoted by brackets. Practically, statistical averages are computed by performing a time average (the ergodic hypothesis). The horizontal average of quantity q is defined as:

$$\langle q \rangle = \frac{1}{\Delta\Omega} \int_{\Delta\Omega} q(r, \theta, \phi) d\Omega, \quad (8)$$

where $d\Omega = \sin\theta d\theta d\phi$ is the solid angle in spherical coordinates.

We decompose the flow quantities into mean and fluctuating components:

$$q = \overline{\langle q \rangle} + q', \quad (9)$$

so that $\overline{\langle q' \rangle} = 0$, by construction. We also introduce Favre averaging, which is a density-weighted average:

$$\widetilde{\langle q \rangle} = \frac{\overline{\langle \rho q \rangle}}{\overline{\langle \rho \rangle}}, \quad (10)$$

and which leads to the decomposition

$$q = \widetilde{\langle q \rangle} + q''. \quad (11)$$

We stress the difference between q' and q'' : the first denotes the fluctuation around the Reynolds average $\overline{\langle q \rangle}$, the second denotes the fluctuation around the Favre average $\widetilde{\langle q \rangle}$.

The density and energy equations lead to their averaged counterpart. From the momentum equations, the three mean-field equations which are consistent with spherical geometry concern the mean radial velocity $\overline{\langle u_r \rangle}$, the mean specific angular momentum along the z -axis $\overline{\langle j_z \rangle}$, and the mean specific KE $\overline{\langle \epsilon_k \rangle}$. By “consistent with spherical geometry” we mean that the resulting equations do not have terms which have an explicit angular dependence, as would for instance have the mean-field equations for u_θ or u_ϕ . The energy equation can be formulated either for the mean specific internal energy $\overline{\langle \epsilon_i \rangle}$, the mean specific total energy $\overline{\langle \epsilon_t \rangle}$, or the mean specific entropy $\overline{\langle s \rangle}$. For completeness, we show all forms. The resulting equations are summarized in Appendix A. We show the equation for $\overline{\langle j_z \rangle}$ although it is “trivial” when rotation is not included; we will not discuss it further here. Note, however, that when rotation is included, the horizontal average as introduced here is not suited because the angular directions are not homogeneous anymore. In this case, similar 1D averaged equations cannot be obtained.

We denote by ∇_r the radial part of the divergence operator in spherical coordinates, i.e., $\nabla_r f = (1/r^2) \partial_r (r^2 f)$. The mean-field equations are characterized by second-order correlations, which stem from the Reynolds/Favre decompositions, as, e.g., the turbulent fluxes which are of the form $\overline{\langle q'' u_r'' \rangle}$ or $\overline{\langle q' u_r' \rangle}$. The equations in Appendix A are written in terms of the averaged Lagrangian derivative

$$\langle \widetilde{D}_t \rangle q = \partial_t q + \overline{\langle u_r \rangle} \partial_r q. \quad (12)$$

The connection with the Eulerian, conservative form is immediate:

$$\overline{\langle \rho \rangle} \langle \widetilde{D}_t \rangle q = \partial_t (\overline{\langle \rho \rangle} q) + \nabla_r (\overline{\langle \rho \rangle} q \overline{\langle u_r \rangle}), \quad (13)$$

where we used the 1D averaged continuity equation.

Connection with the common form of the stellar evolution equations can be made using:

$$\partial_r = 4\pi r^2 \overline{\langle \rho \rangle} \partial_m, \quad (14)$$

$$\langle \widetilde{D}_t \rangle = \partial_t|_m \quad (15)$$

The first equation is the standard relation between the Eulerian derivative at constant radius and the Lagrangian derivative at constant mass shell. The second equation states that $\langle \widetilde{D}_t \rangle$ is exactly the Lagrangian derivative at constant mass. The resulting equations are summarized in Appendix B.

4. RESULTS

Unless stated otherwise, the results in this section are based on models rg.3D.mr and ob.3D.mr. In Section 4.1, we use the mean-field equations developed in Section 3 to analyze our 3D data. These 1D equations provide a powerful framework to analyze the physical processes characterizing the numerical models, and to assess the consistency of the models with the physical equations. Section 4.2 is devoted to the analysis of the turbulent velocity field. We motivate the distinction between “deep

Table 3
Radial Momentum Balance for Model rg.3D.mr—Integral Budget
Over the Convective Zone (g cm s^{-2})

Term	Value	Term	Value
$-\int \langle \bar{\rho} \rangle D_t \langle \widetilde{u_r} \rangle dV$	3.85(28)	$\int \langle \bar{\rho} \rangle \frac{\langle \widetilde{v_h^2} \rangle}{r} dV$	5.62(30)
$-\int \nabla_r \langle \bar{\rho} \rangle \langle \widetilde{u_r'^2} \rangle dV$	6.03(28)	Residual	-5.91(28)
$-\int (\partial_r \langle \bar{p} \rangle - \langle \bar{\rho} \rangle \langle \widetilde{g} \rangle) dV$	-5.66(30)		

convection,” relevant for the red giant models, and “shallow convection,” relevant for the oxygen-burning shell models. We analyze the anisotropy of the Reynolds stresses, which characterizes the asymmetry of the flow, and which motivates a decomposition of the velocity field into a large scale component, characterizing the plumes, and an isotropic component at small scales. We show that the isotropic component provides a natural interpretation of the KE damping in terms of a dissipation in a turbulent cascade. In Section 4.3, we show how the magnitude of pressure fluctuations is related to the stratification of the CZ, which explains the main differences in the mean field analysis between the red giant model and the oxygen-burning shell model. In Section 4.4, we analyze the turbulent fluxes. These are the quantities that should be modeled in a theory of turbulent convection. In Section 4.5, we discuss the KE driving and the turbulent dissipation. We show that in steady state the rate of turbulent dissipation is of the order of the convective luminosity. Section 4.6 is devoted to the red giant models, for which we discuss thermal effects and characterize the overshooting at the bottom of the convective region. Finally, we discuss in Section 4.7 the convergence of our results with resolution, and consider the implications regarding the global dynamics in the numerical models.

4.1. Mean-field Analysis

We use the framework developed in Section 3 to analyze the data from our multi-dimensional simulations, in terms of the radial momentum, KE, and total energy balances. The temporal averaging is performed on the interval $[t_{\text{av}} - \Delta t_{\text{av}}/2, t_{\text{av}} + \Delta t_{\text{av}}/2]$, with t_{av} and Δt_{av} given in Tables 1 and 2 for each model. In practice, we find that averaging the data over more than two turnover timescales yields very similar results. In this section, the models were averaged over the common time period available at different resolutions, namely four turnover timescales (800 days) for the red giant model, and roughly 2.5 turnover timescales (230 s) for the oxygen-burning shell model.

Throughout the paper, we use the lower case letter f to denote turbulent fluxes, $f = \langle \bar{\rho} \rangle \langle \widetilde{u_r'' q''} \rangle$ or $f = \langle \widetilde{u_r' q'} \rangle$, depending on the quantity q .

4.1.1. Radial Momentum Balance

Equation (A6) can be written as:

$$\langle \bar{\rho} \rangle \langle \widetilde{\partial_t} \rangle \langle \widetilde{u_r} \rangle = -\nabla_r \langle \bar{\rho} \rangle \langle \widetilde{u_r'^2} \rangle - \partial_r \langle \bar{p} \rangle - \langle \bar{\rho} \rangle \langle \widetilde{g} \rangle + \langle \bar{\rho} \rangle \frac{\langle \widetilde{v_h^2} \rangle}{r}. \quad (16)$$

This equation is an equation for the mean radial component of the mass flux since by definition $\langle \bar{\rho} \rangle \langle \widetilde{u_r} \rangle = \langle \bar{\rho} u_r \rangle$. The right-hand side (rhs) involves the divergence of the radial component of the Reynolds stress R_{rr} , the balance between the gradient of the mean pressure and the mean gravity force, and a geometric

Table 4
Radial Momentum Balance for Model ob.3D.mr—Integral Budget
Over the Convective Zone (g cm s^{-2})

Term	Value	Term	Value
$-\int \langle \bar{\rho} \rangle D_t \langle \widetilde{u_r} \rangle dV$	-4.55(31)	$\int \langle \bar{\rho} \rangle \frac{\langle \widetilde{v_h^2} \rangle}{r} dV$	1.88(38)
$-\int \nabla_r \langle \bar{\rho} \rangle \langle \widetilde{u_r'^2} \rangle dV$	-2.13(36)	Residual	-4.39(37)
$-\int (\partial_r \langle \bar{p} \rangle - \langle \bar{\rho} \rangle \langle \widetilde{g} \rangle) dV$	-1.42(38)		

term characteristic of spherical geometry in which a horizontal velocity v_h induces a radial acceleration v_h^2/r due to inertia.

The top left panels in Figures 7 and 8 show the radial profiles of these terms in models rg.3D.mr and ob.3D.mr. In both cases, we find the Lagrangian time derivative to be negligible, showing that the balance is in a statistically steady state. The figures show that a slight hydrostatic imbalance is due to the turbulent ram-pressure, with a smaller, but not negligible, contribution from the inertial acceleration due to horizontal motions. Defining

$$p_{\text{turb}} = \langle \bar{\rho} \rangle \langle \widetilde{u_r'^2} \rangle, \quad (17)$$

we find that the ratio p_{turb}/p decreases from $\sim 2 \times 10^{-2}$ at the top of the CZ to $\sim 2 \times 10^{-4}$ at the bottom in the red giant model. In the oxygen burning-shell model, $p_{\text{turb}}/p \sim 10^{-3}$ in the bulk of the CZ, and it decreases rapidly at the boundaries.

In the red giant model, the hydrostatic imbalance corresponds to an inward acceleration of $\sim 3.5\%$ g at the top of the CZ, and an upward acceleration of $\sim 0.05\%$ at the bottom. For the oxygen-burning shell, the results are similar, with values within $\pm 0.2\%$ of g throughout the CZ. Thus, as expected for the deep interior, hydrostatic equilibrium holds, typically to the order of a percent or less. In the photospheric regions the turbulent pressure can significantly affect the hydrostatic balance (Stein & Nordlund 1989).

The top right panels in Figures 7 and 8 (see also Tables 3 and 4) show the balance upon integration over the CZ. The residual is very small in the red giant models, showing good consistency with the physical equations. The oxygen-burning shell models show spurious oscillations at the inner boundary, which are responsible for the non-zero residual seen in the figure. This is due to the steep gradients at this boundary (see Section 4.7), and we have checked that the consistency is very good everywhere else. Progress has been made in dealing with multi-fluids in PPM (Plewa & Müller 1999; Woodward et al. 2008), which may help.

4.1.2. Kinetic Energy Balance

At the first sight, the temporal behavior of the KE shows a high level of complexity (see Figure 2 for the red giant model). The mean KE balance, Equation (A5), allows insight in the dynamics of the turbulent convection (Hurlburt et al. 1986, 1994; Meakin & Arnett 2007). The KE equation involves two turbulent fluxes: the KE turbulent flux $f_k = \langle \bar{\rho} \rangle \langle \widetilde{u_r'' \epsilon_k''} \rangle$ and the acoustic flux $f_p = \langle \bar{p}' u_r' \rangle$. These transport terms characterize the non-locality of turbulent convection. Source terms for KE are the gravitational work due to density fluctuations $W_b = \langle \bar{\rho}' \mathbf{u}' \cdot \mathbf{g} \rangle$, and the work done by pressure fluctuations $W_p = \langle \bar{p}' \nabla \cdot \mathbf{u}' \rangle$, also called “pressure-dilatation.” There is some freedom in the formulation of the KE equation, especially in the expression/splitting of the driving terms, see, e.g., discussions in Nordlund et al. (2009)

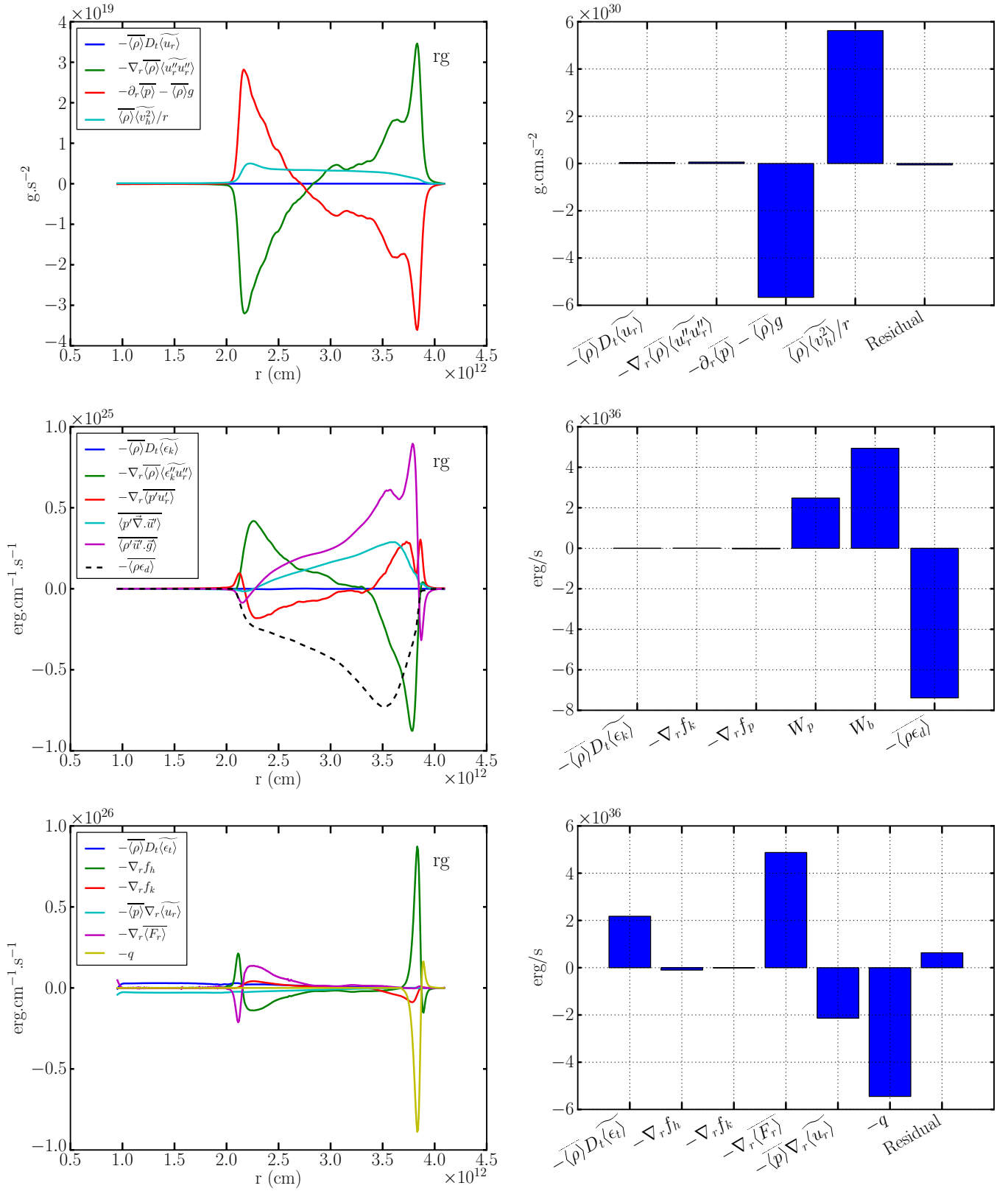


Figure 7. Mean-field analysis for model *rg.3D.mr*, time averaging is performed over 800 days. From top to bottom: radial expansion velocity, kinetic energy, and total energy balance. Left panel: radial profiles of the terms in the balance. For the sake of clarity, each term is multiplied by $4\pi r^2$. As a result, the volume integral of a term is equal to the area below the corresponding curve, and it can be appreciated visually. Right panel: integral budget over the convective zone.

(A color version of this figure is available in the online journal.)

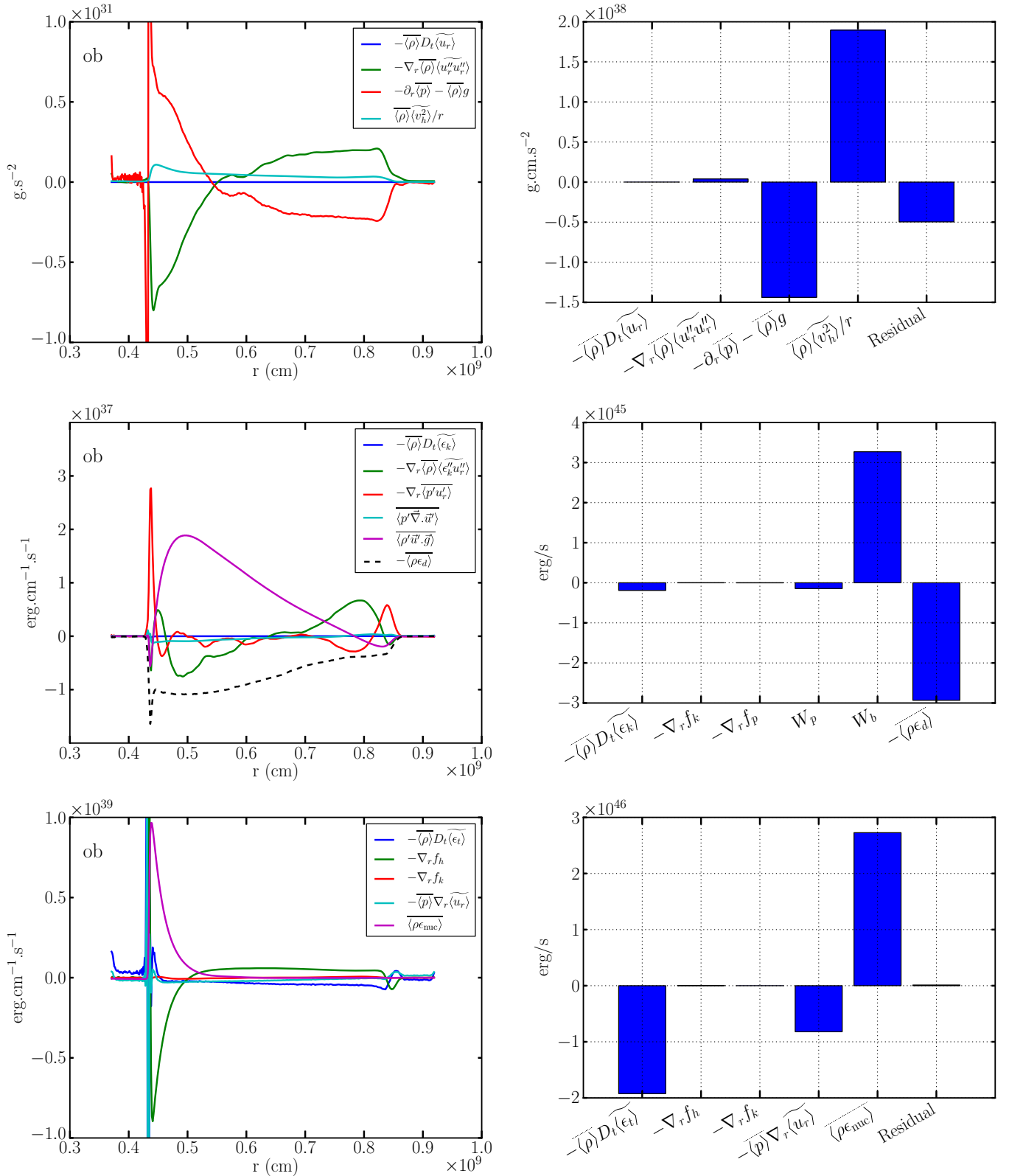


Figure 8. Same as Figure 7 for model ob.3D.mr, with time averaging performed over 230 s.
(A color version of this figure is available in the online journal.)

and Arnett & Meakin (2011). Here we choose to split the driving into W_p and W_b as these are thermodynamically the most fundamental quantities: W_b measures the reversible exchange between KE and potential energy, W_p measures the reversible exchange between KE and internal energy. Furthermore, this

splitting will highlight the differences between the red giant and oxygen-burning shell models. W_b is often called the buoyancy work, an appellation inherited from the Boussinesq literature. In Section 4.5 we present another expression which emphasizes the underlying physical origin of the driving.

Table 5
Kinetic Energy Balance for Model rg.3D.mr—Integral Budget
Over the Convective Zone (erg s⁻¹)

Term	Value	Term	Value
$-\int \langle \rho \rangle D_t \langle \epsilon_k \rangle dV$	-3.47(33)	$\int W_p dV$	2.48(36)
$-\int \nabla_r f_k dV$	-1.61(32)	$\int W_b dV$	4.94(36)
$-\int \nabla_r f_p dV$	-2.68(34)	$-\int \langle \rho \epsilon_d \rangle dV$	-7.39(36)

Table 6
Kinetic Energy Balance for Model ob.3D.mr—Integral Budget
Over the Convective Zone (erg s⁻¹)

Term	Value	Term	Value
$-\int \langle \rho \rangle D_t \langle \epsilon_k \rangle dV$	-1.91(44)	$\int W_p dV$	-1.45(44)
$-\int \nabla_r f_k dV$	-1.96(41)	$\int W_b dV$	3.27(45)
$-\int \nabla_r f_p dV$	-1.04(42)	$-\int \langle \rho \epsilon_d \rangle dV$	-2.93(45)

As discussed in Section 2, in the ILES paradigm we rely on the numerical dissipation at the grid scale to mimic the effect of viscosity. As a result, KE is dissipated at the grid scale, and a sink term $-\rho\epsilon_d$ is introduced in the analysis. We compute each term in the balance equation, and identify the residual with the dissipation. This is valid for conservative methods of advection.

The middle left panels of Figures 7 and 8 show the radial profiles of the different terms in the KE balance for models rg.3D.mr and ob.3D.mr. The inferred dissipation is shown as a black dashed line. The KE balance is in a statistically steady state, as the contribution from the time derivative is negligible. In the red giant model, we find that both W_b and W_p drive (i.e., positive contribution) turbulent motion within the CZ. W_b dominates the driving but the pressure-dilatation term is significant and cannot be neglected. This contrasts with the oxygen-burning shell models where driving is largely dominated by W_b , with no significant contribution from pressure-dilatation. We attribute the importance of W_p in the red giant model to the degree of stratification, which is larger than in the oxygen-burning model (see Sections 4.3 and 4.5). The convective region is bounded by regions where $W_b < 0$. The KE dissipation profile has a large amplitude and is rather evenly distributed over the convective region. There is no local balance between the driving and the dissipation due to transport by the turbulent fluxes. In the red giant model, the net effect of the turbulent KE flux is to transport energy downward in the CZ, whereas in the oxygen-burning shell model KE is transported upward. In the red giant model, the acoustic flux has an opposite effect to the KE flux as it transports KE upwards. It has a more complex behavior close to the boundaries due to an important contribution from waves. In the oxygen-burning shell model the acoustic flux is important close to the boundaries, but it has a negligible effect in the bulk of the CZ.

The middle right panel of Figures 7 and 8 (see also Tables 5 and 6) show the KE integral budget over the CZ. Upon integration on the CZ, we are left with a balance between driving and dissipation:

$$\int W_b dV + \int W_p dV \approx \int \langle \rho \epsilon_d \rangle dV. \quad (18)$$

To obtain the balance described by Equation (18), we have integrated over the unstable region and the convective boundary layers, where dissipation is taking place. The rough balance between driving and dissipation obtained over this region

Table 7
Total Energy Balance for Model rg.3D.mr—Integral Budget
Over the Convective Zone (erg s⁻¹)

Term	Value	Term	Value
$-\int \langle \rho \rangle D_t \langle \epsilon_r \rangle dV$	2.18(36)	$-\int \langle \rho \rangle \nabla_r \langle u_r \rangle dV$	-2.13(36)
$-\int \nabla_r f_h dV$	-1.01(35)	$-\int q dV$	-5.45(36)
$-\int \nabla_r f_k dV$	-1.61(32)	Residual	6.30(35)
$-\int \nabla_r \langle F_r \rangle dV$	4.88(36)		

Table 8
Total Energy Balance for Model ob.3D.mr—Integral Budget
Over the Convective Zone (erg s⁻¹)

Term	Value	Term	Value
$-\int \langle \rho \rangle D_t \langle \epsilon_r \rangle dV$	-1.92(46)	$-\int \langle \rho \rangle \nabla_r \langle u_r \rangle dV$	-8.20(45)
$-\int \nabla_r f_h dV$	4.26(43)	$-\int \langle \rho \epsilon_{nuc} \rangle dV$	2.73(46)
$-\int \nabla_r f_k dV$	-1.96(41)	Residual	1.20(44)

implies that only a small amount of KE is transmitted to the stable zones in form of internal waves, so that the dissipation of waves energy in these regions is small.

4.1.3. Total Energy Balance

We now discuss the total energy balance, Equation (A3). The fluxes that appear in this equation are the radiative flux, the enthalpy flux, and the KE flux:

$$F_r = -\langle \chi \rangle \partial_r \langle T \rangle, \quad (19)$$

$$f_h = \langle \rho \rangle \langle h'' u_r'' \rangle, \quad (20)$$

$$f_k = \langle \rho \rangle \langle \epsilon_k'' u_r'' \rangle. \quad (21)$$

We discuss this form of the energy equation because of its relevance for stellar evolution calculations. For instance, let us consider the simplest case by assuming a steady state and $\langle u_r \rangle = 0$. Multiplying Equation (A3) by $4\pi r^2$ and integrating over radius, one obtains:

$$4\pi r^2 (f_h + f_k + F_r) = L(r), \quad (22)$$

where $L(r) = \int_0^r \langle \rho \epsilon_{nuc} \rangle dV$. Stellar evolution codes use the MLT to compute f_h and ignore f_k . Figure 9 illustrates the different terms in Equation (22) for models rg.3D.mr and ob.3D.mr. The radiative flux is negligible in the oxygen-burning shell models and is therefore ignored. In the red giant model, the radiative luminosity is equal to the stellar luminosity in the radiative zone, and it decreases in the CZ where a large and outward directed enthalpy flux takes over. Furthermore, the red giant model is characterized by a downward directed KE flux reaching an amplitude of roughly 35% of the maximum enthalpy flux. The convective boundary is characterized by a negative, i.e., downward directed, enthalpy flux. This is somewhat counterbalanced by a bump in the radiative luminosity at the same location. The total luminosity is not constant, which means that the model is not in thermal equilibrium. The oxygen-burning shell model is characterized by an upward KE flux, with a maximum amplitude roughly equal to 5% of the maximum enthalpy flux. Neutrino cooling is responsible for the shallow region of negative luminosity. Nuclear burning is more important and dominates L_{nuc} . A net heating results and the system is in thermal imbalance (Equation (22) is not valid in this case).

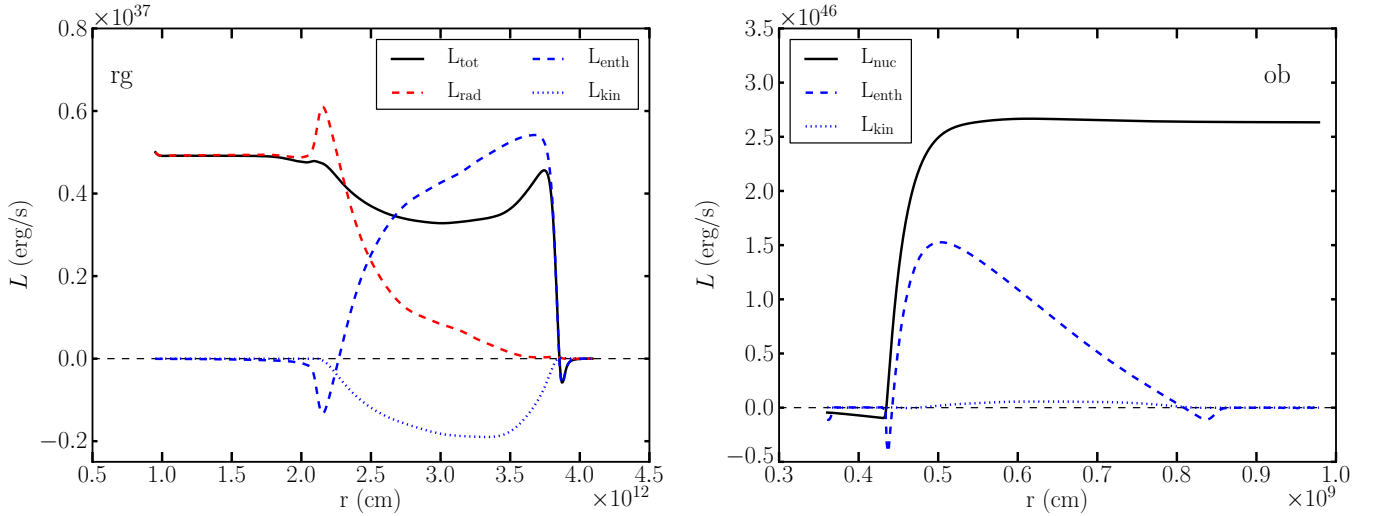


Figure 9. Radial profiles of different luminosities in rg.3D.mr (left panel) and in ob.3D.mr (right panel).
(A color version of this figure is available in the online journal.)

The bottom left panels in Figures 7 and 8 show the different terms of Equation (A3) for models rg.3D.mr and ob.3D.mr. In the red giant case, we introduced in the rhs the Newtonian cooling term q ; see Equation (1). This last term is only important at the top of the CZ, where it mimics the radiative cooling that would take place if we had a realistic photosphere. This convection is driven by cooling at the top. At the bottom of the CZ, there is a rough balance between the radiative and the enthalpy flux. Radiation cools the gas in a shallow layer below the CZ, and heats it at the bottom of the CZ. The radiative cooling in a shallow layer below the CZ is a different manifestation of the bump seen in the radiative luminosity, and this is discussed further in Section 4.6. The discussion of KE flux remains the same as in the previous section: KE is transported downward in the CZ. The oxygen-burning shell model shows a rough balance between nuclear heating and the divergence of the enthalpy flux: convection is driven by a heating from below. It should be noted that the time derivative of the total energy contributes significantly to the balance, as a result from the thermal imbalance. Spurious oscillations are also present at the location of the steep gradients (at the convective boundaries), but we have checked that the consistency was good everywhere else.

The bottom right panels in Figures 7 and 8 show the budget integrals over the CZ for each model (see also Tables 7 and 8). In both cases, a net heating term is present in the red giant due to radiation and in the oxygen-burning shell due to nuclear burning. In the latter, this is counterbalanced by the evolution of the background state through the change in time of the total energy and the $-\langle p \rangle \nabla_r \langle u_r \rangle$ term which is the rate of work by the mean pressure due to a global expansion/contraction of the star. In the red giant model, the radiative heating is mostly balanced by the cooling at the surface. The terms describing a global evolution of the background roughly balance each other and describe how the background state is slowly evolving toward thermal equilibrium (see discussion in Section 4.6).

4.2. The Turbulent Velocity Field

In this section, we analyze the properties of the velocity field, and consider relevant approximations for this field. We

analyze in some detail the anisotropy of the Reynolds stresses. Our results motivate a two component decomposition to the flow, with plumes at large scales and isotropic turbulence at small scales. We show how the isotropic component is related to the observed KE dissipation, consistent with the Kolmogorov cascade.

4.2.1. Approximations for Deep and Shallow Convection

Figures 3 and 6 show that the thermodynamical fluctuations in both stellar models are small relative to the background values. Therefore, for the purpose of analysis, we will often use simplified equations resulting from a linearization around the background state. In such a case, we shall use ρ_0 , P_0 , etc., instead of the notation $\langle \rho \rangle$, $\langle P \rangle$, etc., to emphasize that we are considering the linearized equations.

The linearized continuity equation reads

$$\partial_t \rho' + \nabla \cdot (\rho_0 \mathbf{u}') = 0. \quad (23)$$

Both the red giant and oxygen-burning shell models are characterized by low Mach flows. Low Mach turbulence is an inefficient producer of sound (Lighthill 1952). Therefore, we can neglect $\partial_t \rho'$ in the above equation and focus on fluctuations having a timescale longer than the acoustic timescale (Gough 1969; Dutton & Fichtl 1969). Furthermore,

$$\nabla \cdot (\rho_0 \mathbf{u}') = \rho_0 \nabla_h \cdot \mathbf{u}'_h + \rho_0 \nabla_r u'_r + u'_r \partial_r \rho_0, \quad (24)$$

where we have separated the horizontal flow (subscript h) from the vertical flow. The order of magnitude of the ratio of the third term to the second is:

$$\frac{|u'_r \partial_r \rho_0|}{|\rho_0 \nabla_r u'_r|} \sim \frac{L_u}{H_\rho}, \quad (25)$$

where L_u is the characteristic vertical length-scale of radial velocity perturbations, and $H_\rho = -dr/d \ln \rho_0$ is the density scale-height. For “shallow” convection, this ratio is small and the following approximation is justified:

$$\nabla \cdot \mathbf{u}' = 0, \quad (26)$$

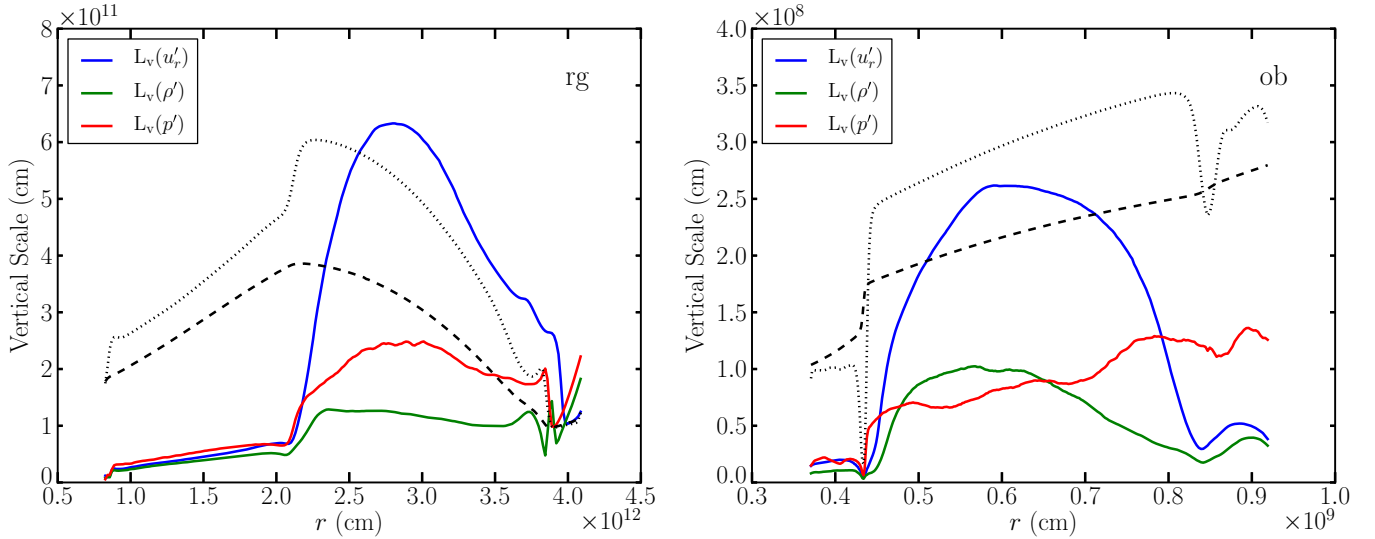


Figure 10. Vertical correlation length-scales for the radial velocity, density and pressure fluctuations in model rg.3D.mr (left panel) and model ob.3D.mr (right panel). The dashed and dotted lines show the pressure and density scale-heights (respectively).

(A color version of this figure is available in the online journal.)

i.e., the turbulent velocity field is solenoidal. Otherwise, for “deep” convection, where $L_u \gtrsim H_\rho$, the appropriate approximation is:

$$\nabla \cdot (\rho_0 \mathbf{u}') = 0. \quad (27)$$

From this relation, we can deduce that

$$\nabla \cdot \mathbf{u}' = \frac{u'_r}{H_\rho}. \quad (28)$$

The dilatation of the velocity field is due to the vertical motion of parcels in the background stratification.

Meakin & Arnett (2007) compute the two-point correlation function of the radial velocity fluctuations:

$$C^V(r, \delta r) = \frac{\overline{(u'_r(t; r, \theta, \phi) u'_r(t; r + \delta r, \theta, \phi))}}{u_{\text{rms}}(r) u_{\text{rms}}(r + \delta r)}, \quad (29)$$

where $u_{\text{rms}}^2 = \overline{(u'^2)}$. The vertical correlation length scale is defined as the width at half maximum of the two-point correlation function C^V . Figure 10 shows the vertical correlation length-scale of the radial velocity fluctuations (among others) computed at each radii in models rg.3D.mr and ob.3D.mr. The figure emphasizes an important difference between the models: in the oxygen-burning shell model, the vertical correlation length-scale is everywhere smaller than the density scale-height, whereas in the red giant model it is larger in most of the CZ. This suggests that the flow in the oxygen-burning shell model is much less affected by the stratification than the red giant model. Therefore, we will adopt the shallow convection approximation Equation (26) to describe the turbulent velocity field in the oxygen-burning shell models. For the red giant models, the appropriate approximation is the one given by Equation (27).

Equations (26) and (27) are the basis for the Boussinesq and anelastic approximations. We stress that for both the oxygen-burning shell and the red giant models, these approximate models of the hydrodynamical equations *should not* be used to model the flow. For instance, the computational domain in the oxygen-burning shell models is not “shallow,” i.e., $(r_{\text{out}} -$

$r_{\text{in}})/H_p > 1$, and in the red giant models the Mach numbers are too large near the surface. However, these approximations provide a useful theoretical framework for the analysis of the results.

4.2.2. Anisotropy of the Reynolds Stresses

We decompose the Reynolds stresses as

$$\overline{(u'_i u'_j)} = \frac{2}{3} \langle \tilde{k} \rangle \delta_{ij} + \langle \tilde{k} \rangle b_{ij}, \quad (30)$$

where $\langle \tilde{k} \rangle = (1/2) \overline{(u'_i u'_i)}$ is the specific turbulent KE and b_{ij} is a trace-less and symmetric tensor that characterizes the anisotropy of the Reynolds stresses. We extract the three eigenvalues ($\lambda_r, \lambda_\theta, \lambda_\phi$) and eigenvectors of b_{ij} at each radii. It can be shown that, for any two eigenvalues α, β , one has $\alpha \geq -2/3$, $\beta \geq -2/3$, and $\alpha + \beta \leq 2/3$.

At each radius, one of the eigenvalue is unambiguously associated with a purely radial eigenvector, and the two other eigenvalues are roughly equal and associated with two purely horizontal eigenvectors. Therefore, the Reynolds stresses are axisymmetric, which is expected as the angular directions are homogeneous in the absence of rotation or magnetic field. The orientation of the horizontal eigenvectors is therefore not physically relevant. The radial profiles of the radial eigenvalue λ_r and of the horizontal eigenvalues λ_θ and λ_ϕ are shown in Figure 11 for models rg.3D.mr and ob.3D.mr. These quantities describe the shape of the Reynolds stress tensor. In the bulk of the CZ, where $\lambda_r > 0$ and $\lambda_\theta = \lambda_\phi < 0$, the shape is “rod-like” as the stress is maximum in the radial direction. Otherwise, when $\lambda_r < 0$ and $\lambda_\theta = \lambda_\phi > 0$, the shape is “disk-like.” The radii at which the transition between the two shapes occurs (and where all eigenvalues cancel) are $r_{\text{in}} \sim 2.2 \times 10^{12}$ cm and $r_{\text{out}} \sim 3.75 \times 10^{12}$ cm in the red giant model, and $r_{\text{in}} = 0.45 \times 10^9$ cm and $r_{\text{out}} \sim 0.85 \times 10^9$ cm in the oxygen-burning shell model. At these radii, the vertical motions are deflected horizontally as they approach the convective boundaries. A second transition radius is seen at $r = 2 \times 10^{12}$ cm in the red giant model and at $r = 0.41 \times 10^9$ cm in the oxygen-burning shell model, below this radius the flow is dominated by waves rather than turbulence.

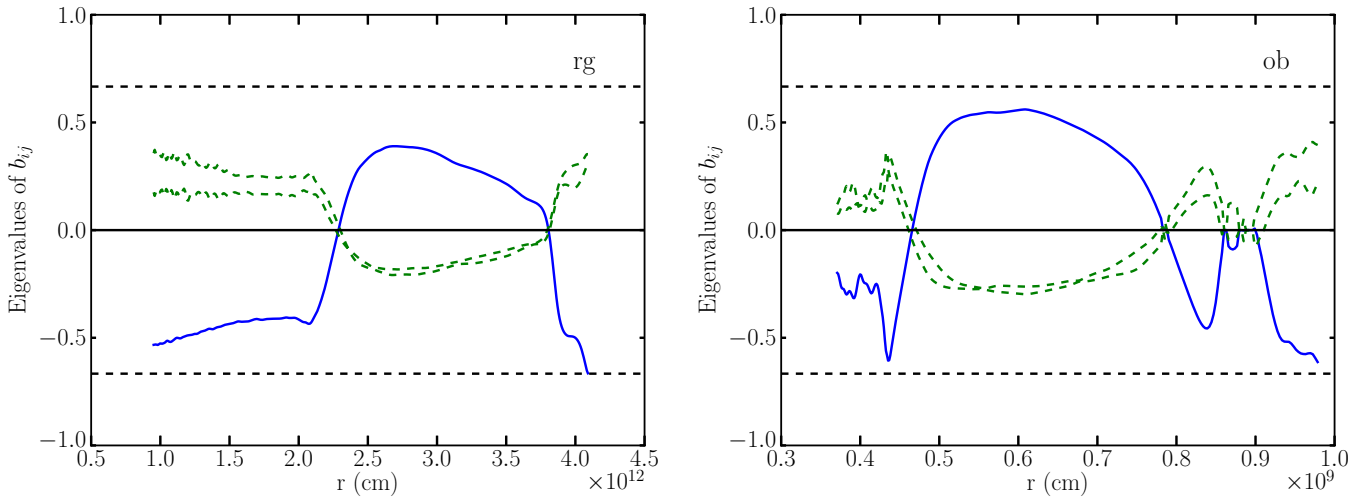


Figure 11. Eigenvalue analysis of the anisotropy tensor b_{ij} for model *rg.3D.mr* (left panel) and model *ob.3d.mr* (right panel). The figures show the radial profiles of the eigenvalues. The continuous line corresponds to the radial eigenvalue, the dashed lines correspond to the horizontal eigenvalues (see text). The two horizontal dashed lines indicate the range $[-2/3, 2/3]$.

(A color version of this figure is available in the online journal.)

The anisotropy of the Reynolds stresses is another manifestation of the two components character of the flow, with convective plumes at large scales that dominate the vertical motion and an isotropic component at small scales. It is essential for the design of turbulence models to better understand the role of the different scales of the flow, for instance in terms of the transport of energy (Cattaneo et al. 1991; Bessolaz & Brun 2011). We leave a detailed analysis for a future publication.

Here, we outline an approach for decomposing the velocity field. We write:

$$u_i = \widetilde{\langle u_i \rangle} + v_i'' + w_i'', \quad (31)$$

where we have split the velocity fluctuation (u_i'' in our usual notation) into a large scale, coherent structures component v_i'' , and an isotropic component w_i'' characterizing the small scales. We then assume that both components have zero averages and are not correlated:

$$\widetilde{\langle v_i'' \rangle} = 0, \quad \forall i, \quad (32)$$

$$\widetilde{\langle w_j'' \rangle} = 0, \quad \forall j, \quad (33)$$

$$\widetilde{\langle v_i'' w_j'' \rangle} = 0, \quad \forall (i, j). \quad (34)$$

With these assumptions, the velocity components correlation tensor can be split into two contributions:

$$\widetilde{\langle u_i'' u_j'' \rangle} = \widetilde{\langle v_i'' v_j'' \rangle} + \widetilde{\langle w_i'' w_j'' \rangle}. \quad (35)$$

Furthermore, we have

$$\widetilde{\langle v_i'' v_i'' \rangle} = 2\tilde{k}_{\text{plumes}}, \quad (36)$$

$$\widetilde{\langle w_i'' w_j'' \rangle} = \frac{2}{3}\tilde{k}_{\text{iso}}\delta_{ij}, \quad (37)$$

with $\widetilde{\langle k \rangle} = \tilde{k}_{\text{plumes}} + \tilde{k}_{\text{iso}}$, where $\tilde{k}_{\text{plumes}}$ and \tilde{k}_{iso} are the specific KE of the plumes and of the isotropic turbulence, respectively. The above hypotheses are not sufficient to uniquely determine the decomposition. Here, it will be enough for our purpose to adopt the approach of Meakin & Arnett (2007): far from the

boundaries, we identify the horizontal flow with the isotropic component. Therefore, as a proxy, we can define \tilde{k}_{iso} by

$$2\tilde{k}_{\text{iso}} = \frac{3}{2}(\widetilde{\langle u_\theta''^2 \rangle} + \widetilde{\langle u_\phi''^2 \rangle}). \quad (38)$$

Furthermore, since $\widetilde{\langle u_\theta''^2 \rangle} \approx \widetilde{\langle u_\phi''^2 \rangle}$, one has

$$\widetilde{\langle v_i'' v_j'' \rangle} \approx 2\tilde{k}_{\text{plumes}}\delta_{i1}\delta_{j1}, \quad (39)$$

with

$$2\tilde{k}_{\text{plumes}} = \widetilde{\langle u_r''^2 \rangle} - \frac{\widetilde{\langle u_\theta''^2 \rangle} + \widetilde{\langle u_\phi''^2 \rangle}}{2}. \quad (40)$$

In the red giant case, the assumption that the small-scale turbulence is isotropic might be questioned owing to the strong stratification. This deserves further investigations. Nevertheless, we will see in the next section that the approach presented here gives consistent results.

4.2.3. Kinetic Energy Damping

The total KE dissipated per unit time is $L_d = \int \overline{\langle \rho \epsilon_d \rangle} dV$; see Tables 1 and 2. The rate of dissipation is not constant in time, but evolves with the flow. In the red giant model, we see a decrease in time of L_d toward the value quoted in the table as the model relaxes toward a quasi-steady state (see the left panel of Figure 2). In the oxygen burning-shell model, L_d increases slowly with time as a result from the global heating due to the imbalance between nuclear heating and neutrino cooling.

As in Arnett et al. (2009), we compute a dissipation length-scale l_d and timescale τ_d as:

$$\int \overline{\langle \rho \epsilon_d \rangle} dV = M_{\text{CZ}} \frac{v_{\text{rms}}^3}{l_d}, \quad (41)$$

$$\tau_d = \frac{E_{\text{K,CZ}}}{\int \overline{\langle \rho \epsilon_d \rangle} dV} = \frac{1}{2} \frac{l_d}{v_{\text{rms}}}, \quad (42)$$

where v_{rms} is computed from the isotropic KE defined in the previous section, i.e., $v_{\text{rms}} = (2\tilde{k}_{\text{iso}})^{1/2}$. This yields $l_d =$

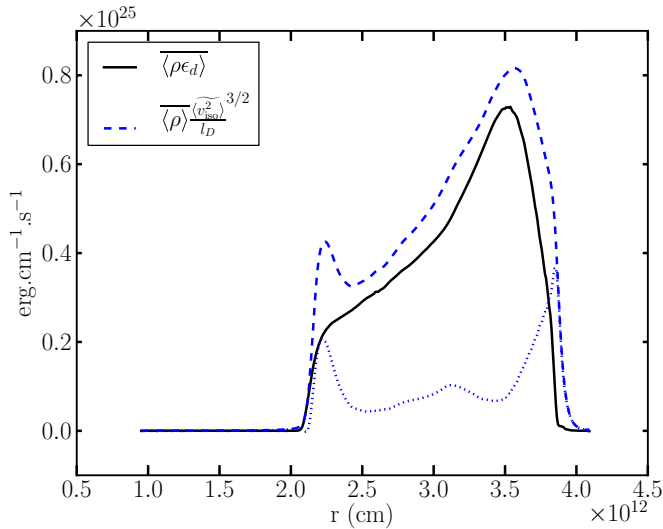


Figure 12. Comparison of the dissipation described by a $\epsilon_k = u^3/\Lambda$ law (dashed line) with the dissipation inferred from the data in model rg.3D.mr (continuous line). The dotted line shows the residual.

(A color version of this figure is available in the online journal.)

7.7×10^{11} cm in the red giant model, and $l_d \sim 0.4l_{CZ}$; and $l_d = 5.5 \times 10^8$ cm in the oxygen burning-shell model, so $l_d \sim l_{CZ}$. Furthermore, $\tau_d \sim 19$ days in the red giant model and $\tau_d \sim 29$ s in the oxygen-burning shell model. In both cases this is much shorter than the convective turnover timescale. As discussed in Arnett et al. (2009), this illustrates the strong dissipative character of turbulent convection.

We now relate the KE dissipation inferred from the numerical simulations with global properties of the flow. The simplest approach is to use the formula for the rate of dissipation in isotropic and homogeneous incompressible turbulence (Pope 2000):

$$\epsilon_d = \frac{u'^3}{\Lambda}, \quad (43)$$

where u' and Λ are the rms velocity and length-scale of the most energetic eddies. Arnett et al. (2009) fit the dissipation in their oxygen-burning shell data with $u' = (2\tilde{k}_{iso})^{1/2}$ and by setting Λ to the dissipation length scale l_d derived above; see the right panel in their Figure 2. In Figure 12, we show that the same approach gives fairly good results for the red giant model as well. The amplitude of the dissipation is slightly overestimated, but the overall shape of the profiles agree very well. This suggests that a somewhat larger value of l_d would give a better fit. The largest discrepancies are found close to the convective boundaries, where \tilde{k}_{iso} is affected by the horizontal flow due to the interaction with the boundaries.

It should be emphasized that this approach works well in our case because we are in a statistically steady state. In situations where the KE changes rapidly, the dissipation rate lags behind the cascade rate given by u^3/Λ due to the time needed to redistribute the KE over the inertial range (Livescu et al. 2009).

4.3. Magnitude of Pressure Fluctuations

A comparison of Figures 3 and 6 shows that $p'/p_0 \sim \rho'/\rho_0$ in the red giant model, whereas the oxygen-burning shell model is characterized by $p'/p_0 < \rho'/\rho_0$. This is related to the background stratification.

Within the framework of the approximations presented in Section 4.2.1, it is possible to obtain an elliptic equation for the pressure fluctuations (see Appendix C):

$$\Delta p' = -\nabla : (\rho_0 \mathbf{u}' \otimes \mathbf{u}') - g \frac{\partial \rho'}{\partial r}. \quad (44)$$

The first term on the rhs describes the generation of pressure fluctuations by the Reynolds stresses, also called the “pseudo-sound.” The second term describes the generation of pressure fluctuations by buoyancy effects. The relative orders of magnitude of the different terms can be written as:

$$\frac{|p'|}{p_0} : \left(\frac{L_p}{L_u} \right)^2 \frac{\rho_0 |u'|^2}{p_0} : \frac{L_p^2}{H_p L_\rho} \frac{|\rho'|}{\rho_0}, \quad (45)$$

where L_p , L_u , and L_ρ are typical length scales for variation of the pressure, velocity, and density fluctuations. We use the vertical correlation length-scales for u'_r , ρ' and p' shown in Figure 10 to estimate the relative magnitude of these effects. We estimate that $L_p^2/L_u^2 \sim 0.2$, $L_p^2/(H_p L_\rho) \sim 2$ in the red giant model, and $L_p^2/L_u^2 \sim 0.1$, $L_p^2/(H_p L_\rho) \sim 0.4$ in the oxygen-burning shell model. Although these estimates are only qualitative, they suggest that the pseudo-sound term is not the dominant source of pressure fluctuations in the CZ (the dashed line in Figures 3 and 6 falls below the pressure curve after multiplication by L_p^2/L_u^2). Therefore, pressure fluctuations are mainly due to buoyancy, and the order of magnitude analysis above shows that magnitude is related to the background stratification. If we loosely assume $L_\rho \sim L_p$ (which is not quite correct in the red giant models), we have

$$\frac{|p'|}{p_0} \sim \frac{L_p}{H_p} \frac{|\rho'|}{\rho_0}, \quad (46)$$

which is in qualitative agreement with the numerical models.

Although the order of magnitude estimates we carried out in this section have no predictive power, they suggest that Equation (44) provides a valuable framework to analyze pressure fluctuations (Chassaing et al. 2002). We plan to push the analysis based on this equation further, with the aim of obtaining more quantitative predictions.

4.4. The Turbulent Fluxes

4.4.1. The Turbulent Mass Flux

The turbulent mass flux is defined as

$$f_m = \overline{\rho' u'_r}. \quad (47)$$

By definition, we have

$$\overline{\langle \rho \rangle \langle u_r \rangle} = \overline{\langle \rho u_r \rangle} = \overline{\langle \rho \rangle \langle u_r \rangle} + \overline{\langle \rho' u'_r \rangle}. \quad (48)$$

The top panels of Figure 13 illustrate this relation in models rg.3D.mr and ob.3D.mr. In the red giant model, one has $\langle u_r \rangle \approx 0$ as the model is close to equilibrium. In this case, Equation (48) implies that the mean flow $\langle u_r \rangle$ counter-balances the mass displaced by turbulence. The oxygen burning-shell model shows a quite significant expansion of the background, i.e., $\langle u_r \rangle > 0$, driven by the imbalance between nuclear burning and neutrino cooling. There is still a mean flow which tends to counteract the effect of the turbulent mass flux.

In the gravity field, the mass displaced by the turbulence induces a work which is one of the KE driving term introduced in Section 4.1.2:

$$W_b = \overline{\langle \rho' \mathbf{u}' \cdot \mathbf{g} \rangle} = -g f_m, \quad (49)$$

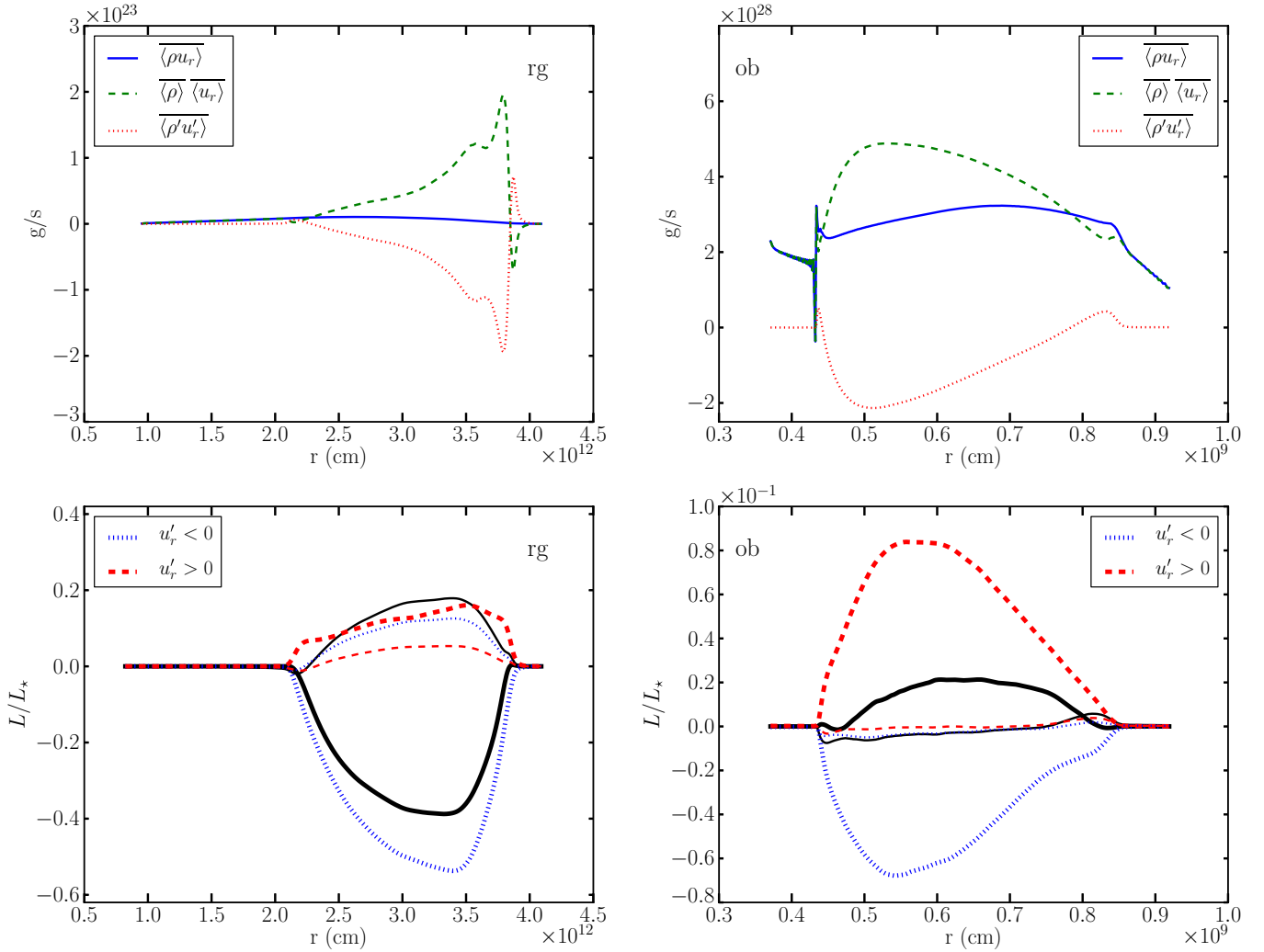


Figure 13. Top panels: decomposition of the average mass flux (see text). Bottom panels: splitting of the kinetic energy (thick lines) and acoustic (thin lines) fluxes into upflow and downflow components (the fluxes have been multiplied by $4\pi r^2$ and normalized by the luminosity). The continuous lines are the total fluxes. Left panels: model rg.3D.mr, right panels: model ob.3D.mr.

(A color version of this figure is available in the online journal.)

where we took g outside of the averaging operator (the Cowling approximation). Note that energetically, Equation (48) implies that when $\langle u_r \rangle \approx 0$, the gravitational work done by the turbulence is canceled by the gravitational work done by the mean flow, so that the total work done by gravity is zero. This is a direct consequence of mass conservation.

4.4.2. Acoustic and Kinetic Energy Fluxes

Assuming that $\langle \rho \rangle \langle \widetilde{D}_t \rangle \langle \widetilde{\epsilon}_k \rangle = 0$, which is justified by the analysis in Section 4.1.2, the integral version of the KE balance, Equation (A5), reads

$$4\pi r^2(f_k + f_p) = \int_0^r (W_b + W_p - \overline{\rho \epsilon_d}) dV, \quad (50)$$

which simply says that transport by combined KE and acoustic fluxes is the residual between driving and dissipation. It is not an explicit formula for the fluxes since the velocity field also enters in the r.h.s, both in the driving and in the dissipation. When f_p and W_p are negligible, the equation simplifies to Equation (4) of Meakin & Arnett (2010).

The bottom left panel in Figure 13 shows the radial profiles of f_k and f_p in model rg.3D.mr. As discussed in Section 4.1.3, the KE

flux f_k is large and downward directed. The figure shows that f_p is smaller, but not negligible, and upward directed. Furthermore, we show in the figure the splitting of f_k and f_p into the downflow ($u'_r < 0$) and upflow components ($u'_r > 0$). In both cases, the contribution from the downdrafts dominates significantly. This emphasizes the strong asymmetry of the flow which results from the large stratification. The figure shows that both components of the acoustic flux are positive, i.e., downflows have $p' < 0$ and upflows have $p' > 0$. Since f_p is not negligible and is upward directed (opposite to the KE flux), a better understanding of f_p is necessary to understand what is setting the amplitude of the KE flux. The right panel in Figure 13 shows the KE and acoustic flux in model ob.3D.mr, which are both small compared to the enthalpy flux. The acoustic flux shows a more complex behavior than in the red giant models. The KE flux is upward directed, and shows a large cancellation due to the approximate symmetry between upflows and downflows. Meakin & Arnett (2010) experimented with the oxygen burning shell models by changing from a heating from below to a cooling from above, and found that the KE flux reversed direction (see their c1 model). Qualitatively, this change of behavior is explained by the different direction of propagation of plumes, which propagate

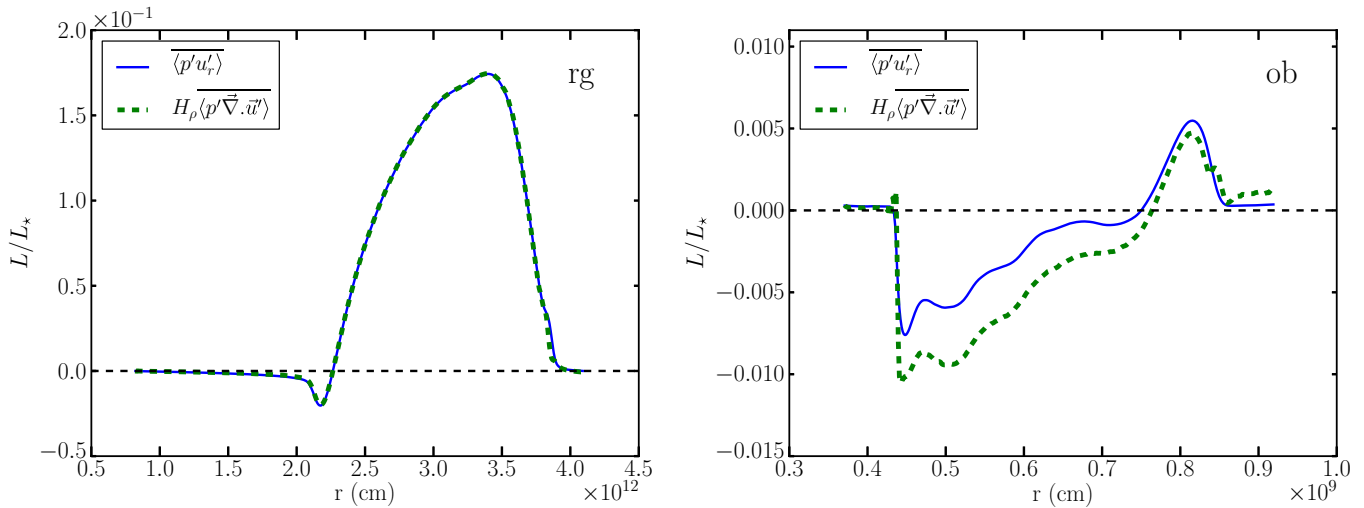


Figure 14. Comparison between the acoustic flux $f_p = \langle p'u'_r \rangle$ and pressure-dilatation $W_p = \langle p' \nabla \cdot \mathbf{u}' \rangle$ multiplied by the density scale-height H_ρ . Both terms were multiplied by $4\pi r^2$ and normalized by the stellar luminosity. Left panel: model rg.3D.mr, right panel: model ob.3D.mr.

(A color version of this figure is available in the online journal.)

downward when triggered by cooling at the top, as in the red giant model.

Finally, multiplying Equation (28) by p' and taking the average one obtains:

$$f_p = \overline{\langle p'u'_r \rangle} = H_\rho \overline{\langle p' \nabla \cdot \mathbf{u}' \rangle} = H_\rho W_p. \quad (51)$$

The left panel of Figure 14 shows that this relation holds to a very good degree in the red giant model, validating a posteriori the use of the anelastic approximation (Section 4.2.1). Equation (51) is very similar to Equation (49): they both connect a flux, f_m and f_p , to a KE source term, W_b and W_p . For f_p and W_p this is true only within the anelastic approximation. We will come back to this in Section 4.5. For the oxygen-burning shell model, consistently with the approximation $\nabla \cdot \mathbf{u}' = 0$ introduced in Section 4.2.1, we consider that $W_p \approx 0$ which is a good approximation. f_p is more complex than in the red giant model, where it is dominated by stratification effects. The right panel of Figure 14 shows that the effects of stratification, as described by the anelastic approximation, reproduce the gross features of f_p , but that other effects contribute. This could be due to pressure perturbations related to boundary effects, or to the background expansion, and requires further investigation.

Note that we have the following relation:

$$\left\langle \frac{p'}{\rho_0} \nabla \cdot (\rho_0 \mathbf{u}') \right\rangle = W_p - \frac{f_p}{H_\rho}, \quad (52)$$

which characterizes the deviation from the anelastic approximation.

4.4.3. Splitting of the Enthalpy Flux

The enthalpy flux describes the transport of heat by convection and is therefore important for stellar interior modeling. In this section, we use thermodynamical relationships to study its relation to other turbulent fluxes. As two state variables are sufficient to determine the thermodynamic state, different expressions for the enthalpy flux can be derived. We choose the pressure as one of the variables, as pressure fluctuations play

a different role in the two stellar models presented here. For the other variable, we will consider density, entropy, and temperature, respectively. For the oxygen-burning shell model, we describe composition effects in terms of the average number of nucleons A and free electrons Z per nucleus.⁶ For the red giant model, these terms are zero because the composition was uniform.

Formally, the turbulent enthalpy flux is defined as $f_h = \overline{\langle \rho \rangle \langle h'' u_r'' \rangle}$, but we have checked that it is identical to $f_h = \overline{\langle \rho \rangle \langle h' u_r' \rangle}$ (the same holds for the other turbulent fluxes). Based on this second form, we first split the enthalpy flux in terms of density, pressure, and composition fluctuations. Assuming that fluctuations of these variables are small,

$$h' = \left. \frac{\partial h}{\partial \rho} \right|_{\rho, A, Z} \rho' + \left. \frac{\partial h}{\partial p} \right|_{\rho, A, Z} p' + \left. \frac{\partial h}{\partial A} \right|_{\rho, p, Z} A' + \left. \frac{\partial h}{\partial Z} \right|_{\rho, p, A} Z', \quad (53)$$

which leads to the following expression:

$$f_h = -\frac{P}{\rho} \frac{\Gamma_1}{\Gamma_3 - 1} \overline{\langle \rho' u_r' \rangle} + \frac{\Gamma_3}{\Gamma_3 - 1} \overline{\langle p' u_r' \rangle} + \rho \left. \frac{\partial e}{\partial A} \right|_{\rho, p, Z} \overline{\langle A' u_r' \rangle} + \rho \left. \frac{\partial e}{\partial Z} \right|_{\rho, p, A} \overline{\langle Z' u_r' \rangle}, \quad (54)$$

where the coefficients are evaluated using the background state. This relation illustrates how the enthalpy flux can be decomposed into separate contributions from the turbulent mass flux, the acoustic flux, and composition fluxes. The top panels in Figure 15 show how this decomposition compares with the numerical data. We find that decomposition (54) holds to an excellent degree of approximation. In the red giant model, both the terms related to density and pressure fluctuations contribute, whereas in the oxygen-burning shell model, the term related to density fluctuations provides the main contribution.

⁶ If the composition variables $Y = 1/A$ and $Y_e = Z/A$ are used, most of the effect is concentrated in the single variable Y . Y_e is almost constant in the oxygen-burning shell.

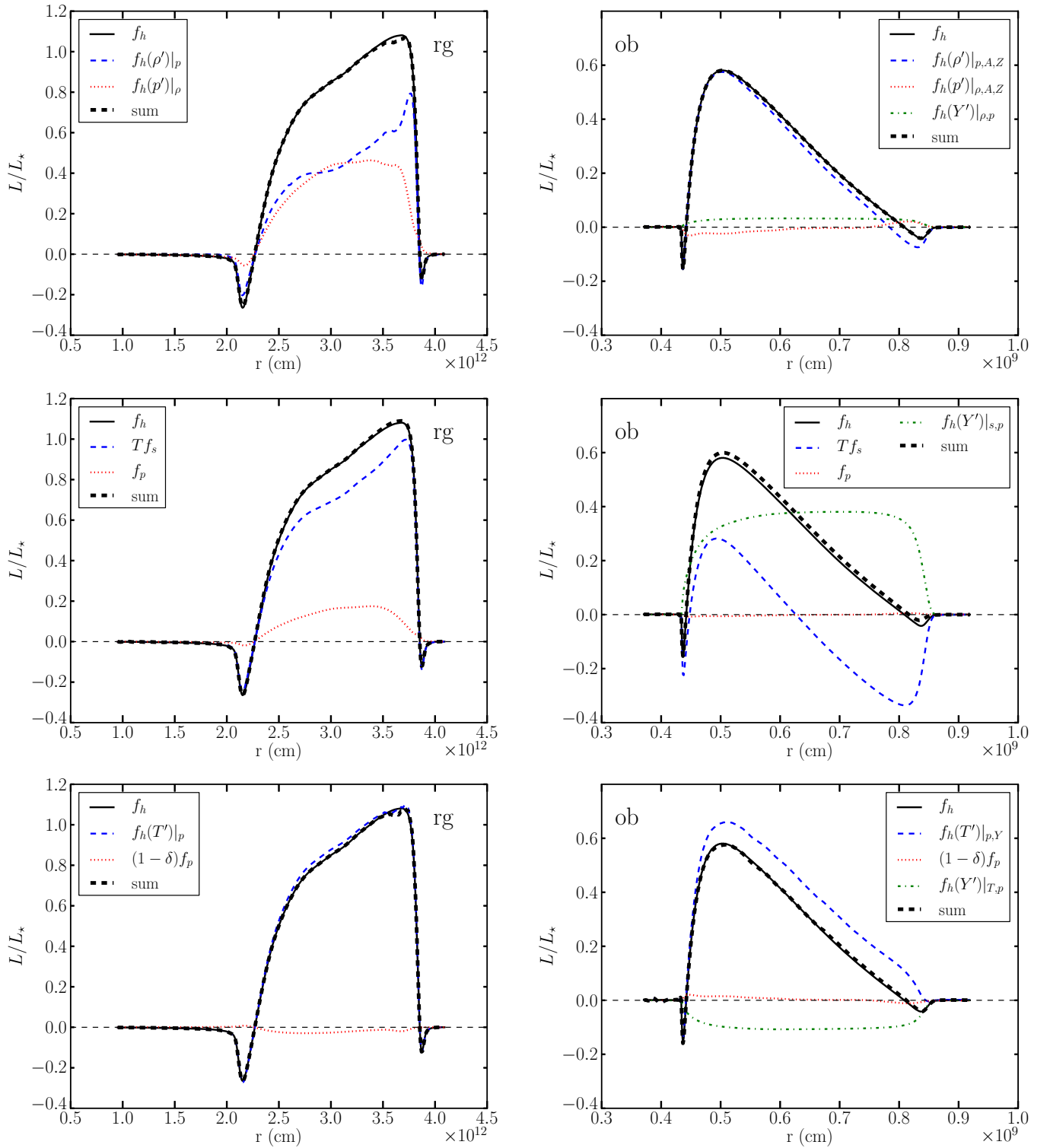


Figure 15. Splitting of the enthalpy flux in models rg.3D.mr (left) and ob.3D.mr (right). Top panels: decomposition with Equation (54). Middle panels: decomposition with Equation (56). Bottom panels: decomposition with Equation (57). $f_h(Y')$ represents the sum of the composition terms due to A' and Z' . The different terms are multiplied by $4\pi r^2$, and normalized to the model luminosity.

(A color version of this figure is available in the online journal.)

A second way to split the enthalpy flux is by introducing the entropy flux in place of the turbulent mass flux. In this approach, we start from

$$h' = Ts' + \frac{1}{\rho} p' + \frac{\partial h}{\partial A} \bigg|_{s,p,Z} A' + \frac{\partial h}{\partial Z} \bigg|_{s,p,A} Z', \quad (55)$$

which, by the same arguments as above, leads to

$$f_h = Tf_s + f_p + \rho \frac{\partial h}{\partial A} \bigg|_{s,p,Z} \overline{\langle A' u_r' \rangle} + \rho \frac{\partial h}{\partial Z} \bigg|_{s,p,A} \overline{\langle Z' u_r' \rangle}. \quad (56)$$

The middle panels in Figure 15 show how this relation compares with the numerical data. In both models, the agreement is very good. In the red giant model, the enthalpy flux mainly results from the entropy flux, with a non-negligible contribution from the acoustic flux. In the oxygen-burning shell models, the contributions from both the entropy and composition fluxes are important. Comparing this with the first splitting, it illustrates that density fluctuations are here both due to thermal effects (i.e., entropy fluctuations) and composition effects.

Finally, it is useful to write the decomposition of the enthalpy flux by introducing temperature fluctuations, one obtains:

$$f_h = \rho c_p \overline{\langle T' u_r' \rangle} + (1 - \delta) f_p + \rho \frac{\partial h}{\partial A} \bigg|_{T,p,Z} \overline{\langle A' u_r' \rangle} + \rho \frac{\partial h}{\partial Z} \bigg|_{T,p,A} \overline{\langle Z' u_r' \rangle}. \quad (57)$$

where $\delta = \alpha T$, with α the coefficient of thermal expansion at constant pressure. In the literature, $\rho c_p \overline{\langle T' u_r' \rangle}$ is often considered as the enthalpy flux. Formally, this is correct only when $\delta = 1$ (e.g., polytropic gas) or $f_p = 0$, and when composition effects are neglected. The left bottom panel in Figure 15 shows that $\rho c_p \overline{\langle T' u_r' \rangle}$ yields a very good approximation of f_h in the red giant model. The right-bottom panel illustrates that in the oxygen-burning shell model, composition effects are significant in this decomposition.

4.5. Kinetic Energy Driving in Compressible Fluids and Turbulent Dissipation in the Convective Zone

In Section 4.1.2, we expressed the driving of KE in terms of W_b , related to density fluctuations, and W_p , related to pressure fluctuations. However, both density and pressure fluctuations arise from different physical processes: thermal effects (i.e., entropy fluctuations), dynamical effects (e.g., compressibility), and composition effects. This leads to a different expression of KE driving, as shown below.

In the linearized velocity equation, the acceleration on the rhs is

$$\mathbf{a} = -\frac{1}{\rho_0} \nabla p' + \frac{\rho'}{\rho_0} \mathbf{g}; \quad (58)$$

see Appendix C. It can be also written as

$$\mathbf{a} = -\nabla \frac{p'}{\rho_0} + \left(\frac{\rho'}{\rho_0} - \frac{H_p}{H_p} \frac{p'}{P_0} \right) \mathbf{g} \quad (59)$$

(Braginsky & Roberts 1995). The physical meaning of the first term can be elucidated by computing its work:

$$-\rho_0 \mathbf{u}' \cdot \nabla \frac{p'}{\rho_0} = -\nabla \cdot (p' \mathbf{u}') + \frac{p'}{\rho_0} \nabla \cdot (\rho_0 \mathbf{u}') \quad (60)$$

This term gives rise to the transport by the acoustic flux and to a source term which is related to the deviation from the anelastic approximation (see Equation (52)). This last term will contribute only when compressible effects become important, i.e., for $M_s \gtrsim 1$.

We identify the second term in Equation (59) with the buoyancy force, written in terms of density and pressure fluctuations.

It can be written as:

$$\frac{\rho'}{\rho_0} - \frac{H_p}{H_p} \frac{p'}{P_0} = \left(\frac{\rho'}{\rho_0} - \frac{1}{\Gamma_1} \frac{p'}{P_0} \right) - \frac{\delta}{\rho_0 c_p g} \frac{ds_0}{dz} p', \quad (61)$$

where we used

$$\frac{1}{H_p} - \frac{1}{\Gamma_1 H_p} = \frac{\delta}{c_p} \frac{ds_0}{dz}. \quad (62)$$

This term characterizes the deviation from adiabaticity of the background. We can make the connection with entropy and composition fluctuations, since we have the thermodynamical relationship

$$\frac{\rho'}{\rho_0} - \frac{1}{\Gamma_1} \frac{p'}{P_0} = -\frac{\delta}{c_p} s' + \frac{\delta}{c_p} \frac{\partial s}{\partial y_i} \bigg|_{\rho,p} y_i', \quad (63)$$

with $y_i' \equiv A, Z$ (with an implicit summation, $y_1 = A, y_2 = Z$).

Using these relations, the total KE driving $W_b + W_p$ can be written as

$$\begin{aligned} W_p + W_b = & \frac{\nabla_{\text{ad}}}{H_p} T f_s \quad \text{Thermal effects} \\ & - \frac{\nabla_{\text{ad}}}{H_p} T \frac{\partial s}{\partial y_i} \bigg|_{\rho,p} f_{y_i} \quad \text{Composition effects} \\ & + \frac{\delta}{c_p} \frac{d\langle s \rangle}{dz} f_p \quad \text{Background effects} \\ & + \left(W_p - \frac{f_p}{H_p} \right), \quad \text{Compressibility effects} \end{aligned} \quad (64)$$

where we used $(\delta g / c_p T) = (\nabla_{\text{ad}} / H_p)$. The first two contributions in Equation (64) can be also written in terms of the turbulent mass flux and acoustic flux thanks to Equation (63). The first three terms are related to buoyancy, which contrasts with the usual designation of W_b as the “buoyancy” driving. Figure 16 illustrates this splitting of the driving for the numerical models. In our cases, both the deviation from adiabaticity and the compressibility effects are negligible. In the red giant model, there are no compositional effects and the above formulation is the most convenient as it expresses the driving only in terms of the entropy flux. In the oxygen-burning shell model, composition effects are important. However, since $p' / P_0 < \rho' / \rho_0$, the driving can be expressed in terms of density fluctuations mainly. This is similar to the comment made with the right panels in Figure 15.

Finally, we can relate the enthalpy flux to the KE driving. In the oxygen-burning shell case, we have from Equation (54):

$$f_h \approx -\frac{P}{\rho} \frac{\Gamma_1}{\Gamma_3 - 1} \overline{\langle \rho' u_r' \rangle} = \frac{H_p}{\nabla_{\text{ad}}} W_b, \quad (65)$$

which connects KE driving (since W_p is negligible) with the enthalpy flux. For the red giant case, we have from Equation (64):

$$W_b + W_p = \frac{\nabla_{\text{ad}}}{H_p} T f_s, \quad (66)$$

which we use Equation (56) to obtain:

$$f_h = \frac{H_p}{\nabla_{\text{ad}}} (W_b + \Gamma_3 W_p). \quad (67)$$

When W_p is negligible, this gives Equation (65).

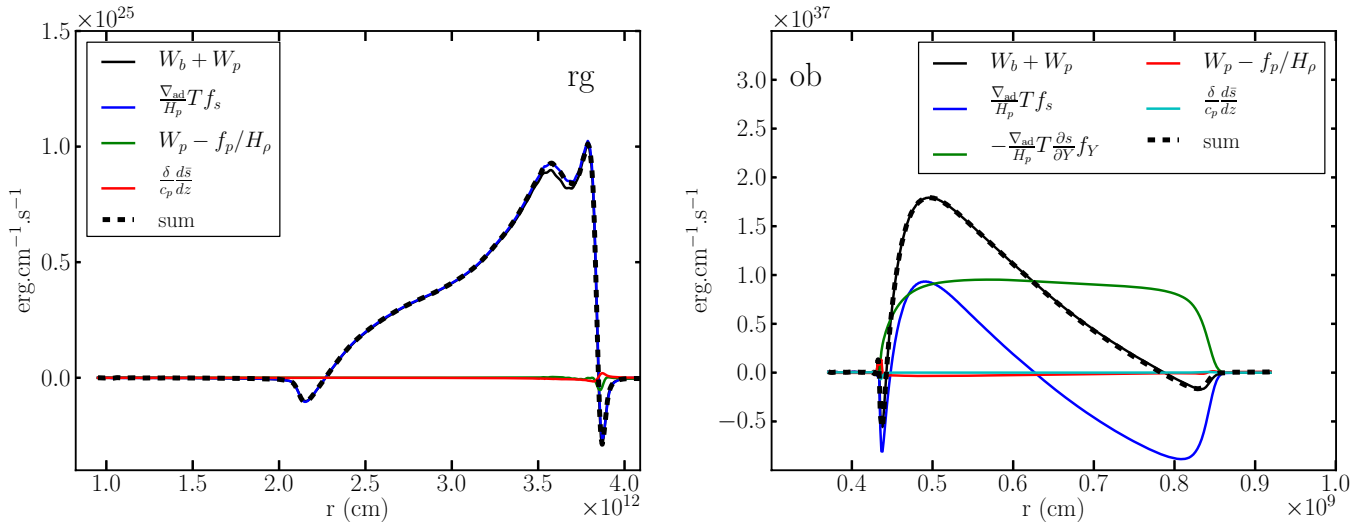


Figure 16. Splitting of the kinetic energy driving for model rg.3D.mr and ob.3D.mr.
(A color version of this figure is available in the online journal.)

In a quasi-steady state, we have $L_d = \int (W_b + W_p) dV$; see Equation (18). Therefore, we can estimate L_d from

$$L_d \approx \int \frac{\nabla_{\text{ad}}}{H_p} f_h dV \approx \bar{\nabla}_{\text{ad}} \bar{L}_c \int_{\text{CZ}} \frac{dr}{H_p} \approx \bar{\nabla}_{\text{ad}} \bar{L}_c n_{H_p}, \quad (68)$$

where $\bar{\nabla}_{\text{ad}}$ is the average value of the adiabatic gradient, \bar{L}_c is the average value of the enthalpy luminosity ($4\pi r^2 f_h$) over the CZ, and n_{H_p} is the number of pressure scale-heights in the CZ. This overestimates L_d when W_p is not negligible because of the factor $\Gamma_3 > 1$ in Equation (67). Nevertheless, it shows that the turbulent dissipation is of the same order as the convective luminosity. This result was suggested by Hewitt et al. (1975). For instance, in the red giant models, we have: $\bar{L}_c \sim 4 \times 10^{36} \text{ erg s}^{-1}$, $\bar{\nabla}_{\text{ad}} \sim 0.35$, $n_{H_p} \sim 7.8$, which gives $L_d \sim 11 \times 10^{36} \text{ erg s}^{-1}$. In the oxygen-burning shell model, we have: $\bar{L}_c \sim 5 \times 10^{45} \text{ erg s}^{-1}$, $\bar{\nabla}_{\text{ad}} \sim 0.245$, $n_{H_p} \sim 2$, which gives $L_d \sim 2.45 \times 10^{45} \text{ erg s}^{-1}$. Both values agree well with the inferred values (see Tables 1 and 2). As expected, the value obtained for the red giant is overestimated.

4.6. Thermal Effects and Overshooting in the Red Giant Model

The Kelvin–Helmholtz timescale is defined as the ratio between the thermal energy and the luminosity of the star:

$$\tau_{\text{KH}} = \frac{E_{\text{int}}}{L_*}, \quad (69)$$

where $E_{\text{int}} = \int \rho \epsilon_i dV$ is the total thermal energy. For the red giant the Kelvin–Helmholtz timescale is $2.1 \times 10^3 \text{ yr}$. This is much longer than our simulations, which span roughly eight years of model time. In fact we are not able to simulate over several thermal timescales, as it would be necessary to ensure that the models have reached thermal equilibrium. This is a common limitation to all numerical simulations of deep convective envelopes that include radiative cooling. One possible way to overcome this problem is to boost the luminosity, thereby bringing the dynamical and thermal timescales closer to each other; e.g., Dobler et al. (2006). A consequence is that the characteristic Mach number of the flow increases. The physical character

of turbulent convection becomes very different, with properties closer to photospheric convection, as compressibility and superadiabatic effects become important. Furthermore, increasing the luminosity implies an increase in the thermal diffusivity,⁷ so that the Péclet number decreases for a given Reynolds number. As discussed below, this will change the behavior at the convective boundaries. For these reasons, we prefer to use a realistic value of the luminosity. As shown in Section 4.1, out of thermal equilibrium behavior can be taken into account in the framework of the mean-field equations.

We characterize our red giant models with a global Péclet number, defined as

$$\text{Pe} = \frac{v_{\text{rms}} l_{\text{CZ}}}{\chi}, \quad (70)$$

where χ is the average value of the radiative diffusivity over the CZ, typically $\chi = 9 \times 10^{13} \text{ cm}^2 \text{ s}^{-1}$. We find $\text{Pe} \sim 5200$ in model rg.3D.mr. This large value characterizes a very efficient transport of heat, and thus a very efficient convection.

In stellar evolution calculations, the locations of the CZ boundaries are based on linear criteria for dynamical stability, namely the Schwarzschild or the Ledoux criteria (the latter takes composition gradients into account). However, due to inertia, fluid parcels can cross this limit. Zahn (1991) presents an analytical investigation of the problem (see also Schmitt et al. 1984; Rempel 2004). Zahn describes as “penetrative convection,” the process in which the superadiabatic region grows in size due to an efficient thermodynamical mixing at the convective boundary. This is the case on the earth, where the planetary boundary layer grows in size during the day. Regarding the connection of the unstable region to the stable interior, Zahn (1991) distinguishes between “overshooting,” in which the transition is made directly in a shallow thermal boundary layer, and “subadiabatic penetration,” in which the penetrative flow first establishes a nearly adiabatic, yet stable, region below the CZ. Zahn (1991) suggests that in stellar interiors, owing to large values of the Péclet number, the conditions for subadiabatic penetration are fulfilled.

⁷ This assumes a given temperature stratification characterizing a stellar structure.

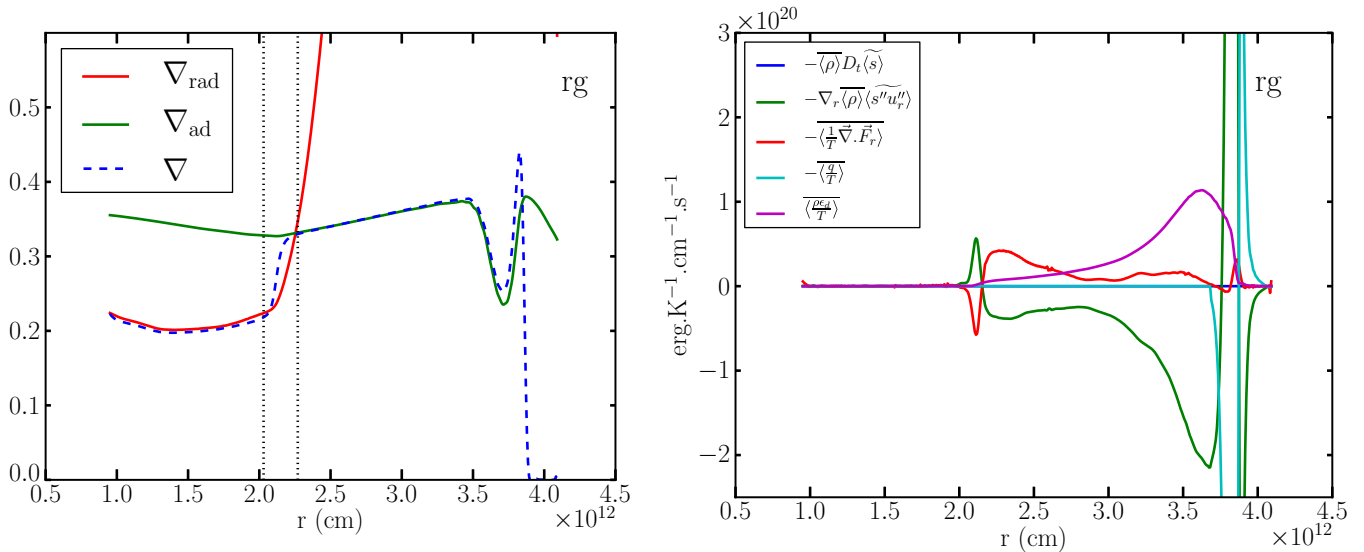


Figure 17. Left panel: dimensionless temperature gradients in model rg.3D.mr, the vertical dotted lines show the bottom convective boundary layer (see the text). Right panel: entropy balance in model rg.3D.mr.

(A color version of this figure is available in the online journal.)

Pioneering numerical studies of the problem are presented in Hurlburt et al. (1986, 1994). Hurlburt et al. (1994) study how subadiabatic penetration/overshooting changes depending on the “stiffness” of the interface, a free parameter of their models. Their models show subadiabatic penetration for low values of the stiffness, whereas for large stiffness they only have an overshooting layer. More recent two-dimensional (2D) work by Rogers & Glatzmaier (2005) arrive to a similar conclusion. Brummell et al. (2002) revisit the problem in 3D, using a similar approach as Hurlburt et al. (1994). None of their 3D models show evidence for a subadiabatic region. The authors argue the reason is the lower filling factor of plumes in 3D turbulent convection, resulting in lower local Péclet numbers. Surprisingly, their numerical models have a smaller convective region than in the initial model.

How do the red giant models compare with these studies? We discuss here only the bottom boundary, as the analysis of the top boundary is undermined by our artificial treatment of the surface cooling. The left panel of Figure 17 shows the dimensionless temperature gradients in model rg.3D.mr. The stratification is very close to adiabatic in the bulk of the CZ, owing to efficient convection. Note that the structure is taken from the averaged model, and that it does not evolve over the time of the simulation.

We show with two dotted lines the region where the enthalpy flux has a negative bump (see the left panel of Figure 9). We identify this region with the convective boundary layer. It has a radial extent of 60% of the local pressure-scale height. The change in sign of the enthalpy flux marks the start of the stably stratified (subadiabatic) region. The radius at which it happens is only slightly smaller than the location of the convective boundary in the initial model: our models do not show evidence for strong convective penetration. Do our models show evidence for subadiabatic penetration? Based on an inspection of the left panel in Figure 17 and of the profile of N^2 (see the right panel in Figure 1), we can see a shallow, nearly adiabatic region which occupies roughly 30% of the convective boundary region. The thermal boundary layer, where the temperature gradient connects smoothly to the radiative value, occupies the remaining 70%. Therefore, we obtain a similar result to Brummell et al.

(2002): this model is characterized by overshooting. The size of our convective boundary layer is on the low side of the range of values resulting from the parameter study of Brummell et al. (2002). This suggests that our boundary is rather “stiff.” Note that this stiffness is a natural outcome of our models, and not an input parameter as in the above-mentioned studies. Furthermore, we have a realistic thermal conductivity profile, depending on density and temperature rather than only on depth.

Following Zahn (1991), Brummell et al. (2002) suggest that they would obtain subadiabatic penetration by modeling higher Péclet number flows. The oxygen-burning shell models have a formally infinite Péclet number,⁸ as thermal diffusion is negligible, and give an insight into the large Péclet number limit. As discussed in detail in Meakin & Arnett (2007), the oxygen-burning shell models show evidence for “turbulent entrainment.” The physical process is one in which the turbulent KE present at the boundary is converted to potential energy as it draws material into the convection zone, mainly through shear instabilities and wave breaking. As a result, the stratification is weakened, and this leads a steady increase in the size of the CZ; see Figure 4 in Meakin & Arnett (2007). As such, this is the same effect as the convective penetration discussed above. However, convective penetration seems to be usually thought as being due to the combined effect of large scale plumes, whereas turbulent entrainment describes the continuous erosion by the small scale turbulence at the interface. Both effects have the same signature: a negative buoyancy work ($W_b < 0$). In the first case, it results from buoyancy braking of the plumes; in the second case, it results from the work the flow is doing against gravity in the process of mixing the stable layer material. These effects are not easy to distinguish in numerical simulations, and both may contribute. Meakin & Arnett (2007) characterize the entrainment rate at convective boundaries based on the bulk Richardson number Ri_B , which measures the stiffness of the interface by taking turbulence into account. This elucidates

⁸ Being negligible, radiative diffusion was removed from the code for increased efficiency.

the behavior of the convective boundary at very large Péclet numbers.

At lower Péclet numbers, how do non-adiabatic effects modify this process? The convective boundary layer in the red giant models is characterized by $W_b < 0$ and $W_p < 0$; see the middle left panel of Figure 7. The figure shows that W_b is dominant: KE is mostly converted into potential energy. Furthermore, the bottom left panel of Figure 7 shows that the divergence of the enthalpy flux leads to heating in the convective boundary layer. This is better analyzed in the framework of the entropy balance, Equation (A4), which is shown in the right panel of Figure 17. In the overshooting layer, the divergence of the entropy flux heats (note that in the overshooting layer $f_h \approx Tf_s$; see the middle left panel in Figure 15). However, it is compensated by cooling from radiation. As a consequence, a quasi-steady state in which non-adiabatic processes counter-balance the effects of turbulent entrainment is possible: the convective region does not increase in size as it does in the oxygen burning case where radiative effects are negligible. The bump in the radiative luminosity is another manifestation of this process. This can be seen also on the left panel in Figure 17, where the convective boundary is characterized by a temperature gradient that is subadiabatic yet super-radiative:

$$\nabla_{\text{rad}} < \nabla < \nabla_{\text{ad}}. \quad (71)$$

Zhang et al. (2012) show how taking this effect into account improves the agreement of solar models with helioseismology data (see also Christensen-Dalsgaard et al. 2011).

Overshooting and subadiabatic penetration correspond to “thermally inhibited” turbulent entrainment/penetrative convection. Subadiabatic penetration requires large Péclet numbers. The estimate given by Equation (70) maybe misleading, as the scales that are involved in the subadiabatic penetration process can be much smaller, and characterized by lower “turbulent” Péclet numbers. Furthermore, the bulk Richardson number might be relevant for subadiabatic penetration as well. A better understanding of the relative effects of the sporadic plumes (Meakin & Arnett 2007; Arnett et al. 2009) that hit the convective boundary and of the continuous erosion by the turbulence is necessary. We suspect that these concepts could shed new light on the results obtained in Brummell et al. (2002).

4.7. Comparison of Different Resolutions

We have performed the various analysis presented in the previous sections for different resolutions and found good agreement, as shown for instance by the various quantities summarized in Tables 1 and 2. We have not found any significant deviation in the physical results that could stem from resolution issues. The oxygen-burning shell models at the lowest resolution (ob.3D.lr) shows spurious oscillations in some averaged quantities. This seems to be related with difficulties Riemann-based solvers have with stratification at low resolution. Even in this case, both the profiles and amplitudes of these quantities are actually in good agreement with the results obtained from higher resolutions which are free of these problems. However, we do not have convergence in the mean fields in the narrow region of steep gradients at the base of the oxygen-burning shell, which are unresolved in the models considered here. There, the dissipation and compositional mixing are affected at the grid scale by the numerical algorithm, which undermines the RANS analysis. The Riemann solver replaces a steep gradient by a con-

tact discontinuity while the RANS analysis requires continuity; this issue requires further study, although the general behavior is relatively sane and the discrepancy localized.

Within the convective region, the mean-field analysis shows robust behavior regarding resolution. The most resolution sensitive diagnostic might be the KE dissipation, which in our models is purely due to numerics at the grid scale. Figure 18 compares the KE balance in models rg.3D.lr and rg.3D.mr, and models ob.3D.mr and ob.3D.hr. The balance looks nearly the same at different resolutions. The KE dissipation profiles are very similar, although the resolutions differ by a factor of two. This suggests that the KE dissipation is set by the large scale properties of the flow, and does not depends on the physics at small scales (here the grid scale). We interpret this as an indication that the dynamics in the turbulent CZ is governed by the large scale dynamics, characterized by the coherent plumes which are well resolved even at our lowest resolution. This is consistent with the picture of the turbulent cascade (Richardson 1922; Kolmogorov 1941): at large Reynolds numbers the rate of dissipation is set by the energy injection at large scale, and is independent of the value of the viscosity. This is the so-called “dissipation anomaly.” The viscosity sets the scale at which dissipation occurs, here the grid scale.

The turbulent regime obtained in numerical simulations (ours and others) is characterized by coherent plumes which propagate (upward or downward) over a significant fraction of the convective region, if not the whole region. They govern the large scale dynamics and are key in guiding the modeling of the highly non-local and non-isotropic transport properties of the flow (see, e.g., Rempel 2004; Lesaffre et al. 2005; Belkacem et al. 2006; Kupka & Robinson 2007; Meakin & Arnett 2007). However, one should bear in mind that our numerical simulations have non-dimensional numbers (e.g., Re, Pr, Ra) which are orders of magnitude different from the values relevant to stellar hydrodynamics. Figure 19 shows snapshots of the flow in the oxygen-burning shell model for three different resolutions. Although the flow is characterized by structures at smaller and smaller scales, we do not see any evidence for a different global behavior of the flow. Whether a transition to a different regime occurs at (much) larger resolution is an outstanding problem. A similar question arises in the study of the simpler, but not less fundamental, Rayleigh-Bénard convection problem. The quest for an understanding and characterization of the “ultimate” state of turbulent Rayleigh-Bénard convection is the focus of much experimental and theoretical work (see reviews by Siggia 1994; Ahlers et al. 2009). Although there are significant physical differences with the stellar case, e.g., stemming from the different nature of boundaries, the extremely low values of the Prandtl number, or the effects of compressibility, it can be expected that a better understanding of turbulent Rayleigh-Bénard convection will provide valuable insight into the turbulent regime at which stellar convection operates (see, e.g., discussion in Spruit 1997). Theoretical studies support the existence of these plumes in stellar CZs (Simon & Weiss 1991; Rieutord & Zahn 1995). Numerical models of the propagation of a plume through the adiabatic stratification show the development of secondary instabilities (Rast 1998; Clyne et al. 2007), but they deal with an idealized situation as the interaction between plumes clearly dominates in our numerical models. Observationally, these plumes are too deep and too small to be detected by current helioseismology measurements; see (Hanasoge et al. 2012) and references therein.

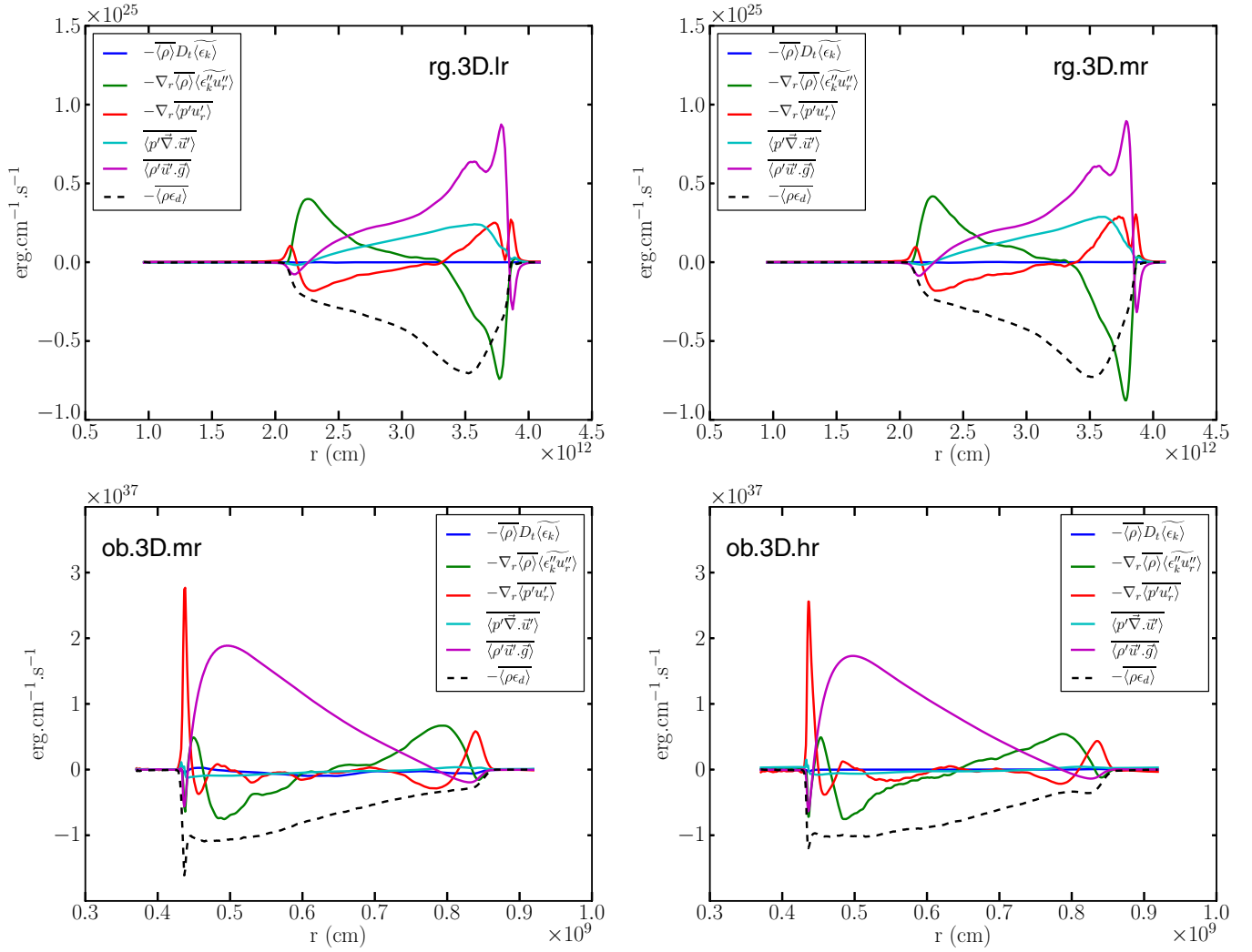


Figure 18. Comparison of the kinetic energy balance for different resolutions. Top panels: models rg.3D.lr and rg.3D.mr. Bottom panels: models ob.3D.mr and ob.3D.hr. (A color version of this figure is available in the online journal.)

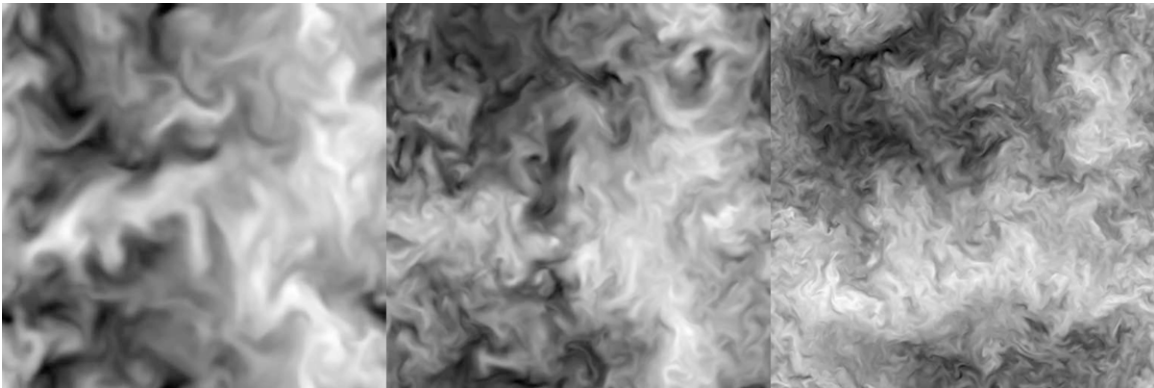


Figure 19. Instantaneous snapshots of the radial velocity field in an horizontal plane in the middle of convective zone for models ob.3D.lr, ob.3D.mr, ob.3D.hr (from left to right). Light tones indicate upflows, dark tones indicate downflows. Each subfigures shows the full angular domain $45^\circ \times 45^\circ$.

5. CONCLUSION

This paper presented 3D models of the turbulent convection in the envelope of a red giant star and in the oxygen-burning shell of a supernova progenitor. The two models differ significantly in their physical properties: they have radically different equations of state, the effects of thermal diffusion is negligible in one

but important in the other, one model is multi-fluid and includes nuclear burning, whereas the other is mono-fluid and has cooling at the surface. Their common point, which is the focus of this work, is the presence of a turbulent CZ which dynamics is controlled by the hydrodynamical equations. Finally, two different numerical methods and codes were used to produce the data. To deal with such a heterogenous set of data, in

Section 3 we developed a set of 1D horizontally-averaged equations that provides a framework for a systematic analysis of hydrodynamical simulations. We showed in Section 4.1 that our numerical models show good consistency with the physical equations, although we identified spurious effects localized in the region of the steep, unresolved gradients present in the oxygen-burning model.

Both our models are characterized by low Mach flows, so that compressible effects are negligible. Similarly, both models have large Péclet number (formally infinite in the oxygen-burning shell case) so that the deviation from adiabaticity is small in the CZ, and has no effect on the dynamics.⁹ However, our analysis is general and applies also to flows with larger Mach number and superadiabatic stratifications, two conditions which are found in photospheric convective regions. We plan to apply a similar analysis to photospheric convection. Our mean-field analysis emphasized very similar behavior in both stellar models, without noticeable dependence on the numerical resolution. Both the radial expansion velocity and KE balances are in a statistically steady state, whereas the total energy balance shows an evolution of the background on a longer timescale. This is due to the clear separation between the dynamical timescale of the system (the turnover timescale) and the nuclear/thermal timescale of the models. The KE dynamics can be understood as a balance between driving at large scales and dissipation at small scales, connected by the turbulent cascade. Understanding the spatial distribution of the driving and of the dissipation is important for insight into the non-locality of convection.

We have shown that the differences between the red giant and oxygen-burning shell models stem mainly from the degree of stratification. This led us to introduce the distinction between “shallow” convection, in which the velocity correlation length-scales are less than the density scale-height, and “deep” convection in which they are of the same order, or larger. As shown in Section 4.3, the effect of stratification on the dynamics can be understood in terms of the magnitude of pressure fluctuations. We discussed how this impacts the mean-field balances: for deep convection pressure-dilatation becomes a non-negligible source of KE, and the acoustic flux contributes to the transport of KE and enthalpy. We showed in Section 4.5 the connection between the transport of enthalpy, the rate of production of turbulent KE, and finally the rate of turbulent dissipation at small scales. This should not be surprising: large scale transport of enthalpy needs motion, motion becomes turbulent, and turbulence dissipates KE at small scales. As a consequence, we find that in a quasi-steady state the rate of dissipation of turbulent KE is of the order of the convective luminosity. This is consistent with the rate of damping of KE inferred from our models. How turbulent dissipation affects stellar evolution is an open question. Figure 20 puts the role of turbulent dissipation in perspective regarding the global conservation of energy. The convective instability taps energy of the unstable stratification and converts potential energy into KE, the work done by the background flow $\langle \bar{u}_r \rangle$ on the mean background $\langle \bar{p} \rangle$ converts internal energy into potential energy, and turbulent dissipation closes the loop by converting KE into internal energy. In a statistically steady state, the amount energy per unit time which is “flowing” in these channels is W_b (see Equations (18) and (48)).

We have discussed in Section 4.6 the overshooting process which is observed in the red giant models. Comparing with the

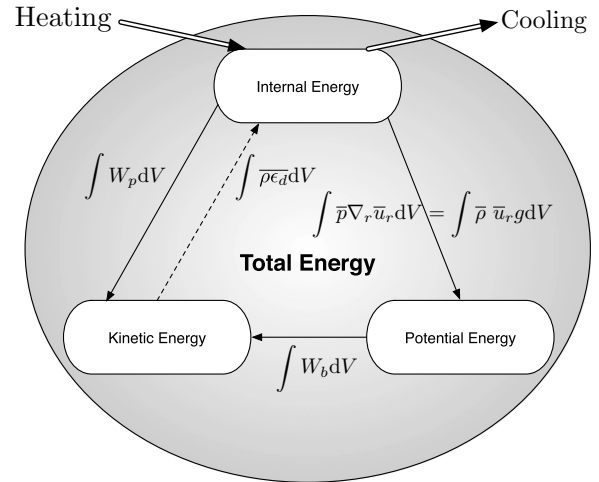


Figure 20. Global energy balance in turbulent convection. The arrow directions are consistent with the labels, i.e., for positive values the energy flows along the arrows. Continuous lines emphasize the reversible character of the processes, whereas the dashed line denotes the irreversible character of kinetic energy dissipation.

oxygen-burning models, we discussed how turbulent entrainment relates to the more classical concepts of overshooting and subadiabatic penetration used in the stellar context. Further investigations on the relative effect of the plumes and turbulent entrainment is desirable.

A turbulent model for stellar convection should be able to reproduce the behavior of the mean-field equations without the need to resort to expensive 3D simulations. In the RANS framework, evolution equations can be derived for the turbulent fluxes. The resulting equations involve higher order terms, for which additional evolution equations can be derived. This leads to a hierarchy of equations which have to be closed with appropriate relations. Future work will apply the same systematic study to higher order equations, aiming at identifying the most important terms to guide the closure strategy (M. Mocák et al., in preparation). We intend to release publicly¹⁰ our RANS analyzed data and provide analysis and plotting subroutines as open source materials.

We plan to extend this work by including rotation and magnetic field. As mentioned in Section 3, the formulation of suitable 1D mean-field equations is not possible when rotation or magnetic field are included. Nevertheless, if non-axisymmetric instabilities are not important, it is possible to average the equations over the azimuthal direction, resulting in a set of 2D mean-field equations. This opens the possibility of performing stellar evolution in 2D, with an appropriate treatment of these effects (in the limit of low rotation rate due to spherical geometry), see, e.g., Deupree (1990, 2001) and Li et al. (2006, 2009). The MUSIC code, which is based on time-implicit methods, provides the ideal framework for that.

M.V. acknowledges support from an International Newton Fellowship from the Royal Society. C.M. and W.D.A. acknowledge support from NSF grant 1107445 at the University of Arizona. This work used the Extreme Science and Engineering Discovery Environment (XSEDE), which is supported by National Science Foundation grant number OCI-1053575.

⁹ In the red giant model, this would not be the case near the surface if it was modeled realistically.

¹⁰ <http://stellarmodels.org>

APPENDIX A

1D RANS EQUATIONS IN LAGRANGIAN FORM

$$\langle \widetilde{D}_t \rangle \langle \widetilde{\rho} \rangle = -\langle \widetilde{\rho} \rangle \nabla_r \langle \widetilde{u}_r \rangle \quad (\text{A1})$$

$$\begin{aligned} \langle \widetilde{\rho} \rangle \langle \widetilde{D}_t \rangle \langle \widetilde{\epsilon}_i \rangle &= -\nabla_r \langle \widetilde{\rho} \rangle \langle \widetilde{\epsilon}_i'' u_r'' \rangle + \nabla_r \langle \widetilde{\chi} \rangle \partial_r \langle \widetilde{T} \rangle - \langle \widetilde{p} \rangle \nabla_r \langle \widetilde{u}_r \rangle \\ &+ \nabla_r \langle \widetilde{\chi}' \partial_r \widetilde{T}' \rangle - \langle \widetilde{p}' \nabla \cdot \widetilde{\mathbf{u}}' \rangle + \langle \widetilde{\rho} \epsilon_{\text{nuc}} \rangle + \langle \widetilde{\rho} \epsilon_d \rangle \end{aligned} \quad (\text{A2})$$

$$\begin{aligned} \langle \widetilde{\rho} \rangle \langle \widetilde{D}_t \rangle \langle \widetilde{\epsilon}_t \rangle &= -\nabla_r \langle \widetilde{\rho} \rangle \langle \widetilde{h}'' u_r'' \rangle - \nabla_r \langle \widetilde{\rho} \rangle \langle \widetilde{\epsilon}_k'' u_r'' \rangle - \langle \widetilde{p} \rangle \nabla_r \langle \widetilde{u}_r \rangle \\ &+ \nabla_r \langle \widetilde{\chi} \rangle \partial_r \langle \widetilde{T} \rangle + \nabla_r \langle \widetilde{\chi}' \partial_r \widetilde{T}' \rangle + \langle \widetilde{\rho} \epsilon_{\text{nuc}} \rangle \end{aligned} \quad (\text{A3})$$

$$\langle \widetilde{\rho} \rangle \langle \widetilde{D}_t \rangle \langle \widetilde{s} \rangle = -\nabla_r \langle \widetilde{\rho} \rangle \langle \widetilde{s}'' u_r'' \rangle - \left\langle \frac{1}{T} \nabla \cdot \mathbf{F}_r \right\rangle + \left\langle \rho \frac{\epsilon_{\text{nuc}} + \epsilon_d}{T} \right\rangle \quad (\text{A4})$$

$$\begin{aligned} \langle \widetilde{\rho} \rangle \langle \widetilde{D}_t \rangle \langle \widetilde{\epsilon}_k \rangle &= -\nabla_r \langle \widetilde{\rho} \rangle \langle \widetilde{\epsilon}_k'' u_r'' \rangle - \nabla_r \langle \widetilde{p}' u_r' \rangle \\ &+ \langle \widetilde{p}' \nabla \cdot \widetilde{\mathbf{u}}' \rangle + \langle \widetilde{\rho}' \mathbf{u}' \cdot \mathbf{g} \rangle - \langle \widetilde{\rho} \epsilon_d \rangle \end{aligned} \quad (\text{A5})$$

$$\begin{aligned} \langle \widetilde{\rho} \rangle \langle \widetilde{D}_t \rangle \langle \widetilde{u}_r \rangle &= -\nabla_r \langle \widetilde{\rho} \rangle \langle \widetilde{u}_r'^2 \rangle - \partial_r \langle \widetilde{p} \rangle - \langle \widetilde{\rho} \rangle \langle \widetilde{g} \rangle \\ &+ \frac{\langle \widetilde{\rho} \rangle}{r} (2\langle \widetilde{\epsilon}_k \rangle - \langle \widetilde{u}_r \rangle^2 - \langle \widetilde{u}_r'^2 \rangle) \end{aligned} \quad (\text{A6})$$

$$\langle \widetilde{\rho} \rangle \langle \widetilde{D}_t \rangle \langle \widetilde{j}_z \rangle = -\nabla_r \langle \widetilde{\rho} \rangle \langle \widetilde{j}_z'' u_r'' \rangle \quad (\text{A7})$$

Definitions: density ρ , temperature T , pressure p , velocity \mathbf{u} , radial velocity component u_r , specific internal energy ϵ_i , specific kinetic energy ϵ_k , specific total energy ϵ_t , specific entropy s , specific enthalpy h , z -component of the specific angular momentum $j_z = r \sin \theta u_\phi$, thermal conductivity χ , radiative flux \mathbf{F}_r , gravitational acceleration \mathbf{g} , rate of nuclear energy production ϵ_{nuc} , rate of viscous dissipation ϵ_d . Reynolds decomposition: $q = \langle \widetilde{q} \rangle + q'$, Favre decomposition: $q = \langle \widetilde{q} \rangle + q''$.

APPENDIX B

1D RANS EQUATIONS IN LAGRANGIAN MASS COORDINATE

$$\partial_t r|_m = \langle \widetilde{u}_r \rangle \quad (\text{B1})$$

$$\begin{aligned} \partial_t \langle \widetilde{\epsilon}_i \rangle|_m &= -\partial_m (4\pi r^2 \langle \widetilde{\rho} \rangle \langle \widetilde{\epsilon}_i'' u_r'' \rangle) + \partial_m (4\pi r^2 \langle \widetilde{\chi} \rangle \partial_r \langle \widetilde{T} \rangle) \\ &- \langle \widetilde{p} \rangle \partial_m (4\pi r^2 \langle \widetilde{u}_r \rangle) + \partial_m (4\pi r^2 \langle \widetilde{\chi}' \partial_r \widetilde{T}' \rangle) \\ &- \frac{\langle \widetilde{p}' \nabla \cdot \widetilde{\mathbf{u}}' \rangle}{\langle \widetilde{\rho} \rangle} + \langle \widetilde{\epsilon}_{\text{nuc}} \rangle + \langle \widetilde{\epsilon}_d \rangle \end{aligned} \quad (\text{B2})$$

$$\begin{aligned} \partial_t \langle \widetilde{\epsilon}_t \rangle|_m &= -\partial_m (4\pi r^2 \langle \widetilde{\rho} \rangle \langle \widetilde{h}'' u_r'' \rangle) - \partial_m (4\pi r^2 \langle \widetilde{\rho} \rangle \langle \widetilde{\epsilon}_k'' u_r'' \rangle) \\ &+ \partial_m (4\pi r^2 \langle \widetilde{\chi} \rangle \partial_r \langle \widetilde{T} \rangle) + \partial_m (4\pi r^2 \langle \widetilde{\chi}' \partial_r \widetilde{T}' \rangle) \\ &- \langle \widetilde{p} \rangle \partial_m (4\pi r^2 \langle \widetilde{u}_r \rangle) + \langle \widetilde{\epsilon}_{\text{nuc}} \rangle \end{aligned} \quad (\text{B3})$$

$$\begin{aligned} \partial_t \langle \widetilde{s} \rangle|_m &= -\partial_m (4\pi r^2 \langle \widetilde{\rho} \rangle \langle \widetilde{s}'' u_r'' \rangle) \\ &+ \frac{1}{\langle \widetilde{\rho} \rangle} \left\langle \frac{1}{T} \nabla \cdot \mathbf{F}_r \right\rangle + \frac{1}{\langle \widetilde{\rho} \rangle} \left\langle \rho \frac{\epsilon_{\text{nuc}} + \epsilon_d}{T} \right\rangle \end{aligned} \quad (\text{B4})$$

$$\begin{aligned} \partial_t \langle \widetilde{\epsilon}_k \rangle|_m &= -\partial_m (4\pi r^2 \langle \widetilde{\rho} \rangle \langle \widetilde{\epsilon}_k'' u_r'' \rangle) - \partial_m (4\pi r^2 \langle \widetilde{p}' u_r' \rangle) \\ &+ \frac{\langle \widetilde{p}' \nabla \cdot \widetilde{\mathbf{u}}' \rangle}{\langle \widetilde{\rho} \rangle} + \frac{\langle \widetilde{\rho}' \mathbf{u}' \cdot \mathbf{g} \rangle}{\langle \widetilde{\rho} \rangle} - \langle \widetilde{\epsilon}_d \rangle \end{aligned} \quad (\text{B5})$$

$$\begin{aligned} \partial_t \langle \widetilde{u}_r \rangle|_m &= -\partial_m (4\pi r^2 \langle \widetilde{\rho} \rangle \langle \widetilde{u}_r'^2 \rangle) - 4\pi r^2 \partial_m \langle \widetilde{p} \rangle \\ &- \langle \widetilde{g} \rangle + \frac{1}{r} (2\langle \widetilde{\epsilon}_k \rangle - \langle \widetilde{u}_r \rangle^2 - \langle \widetilde{u}_r'^2 \rangle) \end{aligned} \quad (\text{B6})$$

$$\partial_t \langle \widetilde{j}_z \rangle|_m = -\partial_m (4\pi r^2 \langle \widetilde{\rho} \rangle \langle \widetilde{u}_r'' j_z'' \rangle) \quad (\text{B7})$$

The definitions are the same as in Appendix A.

APPENDIX C

ELLIPTIC EQUATION FOR THE PRESSURE

We start from the momentum equation:

$$\rho_0 (\partial_t \mathbf{u} + \mathbf{u} \cdot \nabla \mathbf{u}) = -\nabla p' + \rho' \mathbf{g}, \quad (\text{C1})$$

where we have neglected density fluctuations in front of the Lagrangian derivative, and we have subtracted the hydrostatic background. Taking the divergence of this equation removes the time derivative both in the Boussinesq ($\nabla \cdot \mathbf{u} = 0$) and in the anelastic ($\nabla \cdot (\rho_0 \mathbf{u}) = 0$) approximations:

$$\nabla \cdot (\rho_0 \mathbf{u} \cdot \nabla \mathbf{u}) = -\Delta p' - g \frac{\partial \rho'}{\partial r}, \quad (\text{C2})$$

where we considered that g was constant. We write this equation as

$$\Delta p' = -\nabla : (\rho_0 \mathbf{u}' \otimes \mathbf{u}') - g \frac{\partial \rho'}{\partial r}. \quad (\text{C3})$$

REFERENCES

- Ahlers, G., Grossmann, S., & Lohse, D. 2009, *RvMP*, **81**, 503
 Alibert, Y., Baraffe, I., Hauschildt, P., & Allard, F. 1999, *A&A*, **344**, 551
 Arnett, D. 1996, *Supernovae and Nucleosynthesis* (1st ed.; Princeton, NJ: Princeton Univ. Press)
 Arnett, D., Meakin, C., & Young, P. A. 2009, *ApJ*, **690**, 1715
 Arnett, W. D., & Meakin, C. 2011, *ApJ*, **741**, 33
 Baraffe, I., & El Eid, M. F. 1991, *A&A*, **245**, 548
 Belkacem, K., Samadi, R., Goupil, M. J., & Kupka, F. 2006, *A&A*, **460**, 173
 Bessolaz, N., & Brun, A. S. 2011, *ApJ*, **728**, 115
 Böhm-Vitense, E. 1958, *ZA*, **46**, 108
 Botchev, M. A., Sleijpen, G. L., & van der Vorst, H. A. 1999, *ApNM*, **31**, 239
 Braginsky, S. I., & Roberts, P. H. 1995, *GAPD*, **79**, 1
 Brummell, N. H., Clune, T. L., & Toomre, J. 2002, *ApJ*, **570**, 825
 Brummell, N. H., Hurlburt, N. E., & Toomre, J. 1996, *ApJ*, **473**, 494
 Buchler, J. R., & Kolláth, Z. 2000, in *Annals of the New York Academy of Sciences: Astrophysical Turbulence and Convection*, Vol. 898, ed. J. R. Buchler & H. Kandrup, **39**
 Canuto, V. M. 1992, *ApJ*, **392**, 218
 Canuto, V. M. 1997, *ApJ*, **482**, 827
 Canuto, V. M. 2011, *A&A*, **528**, 76
 Canuto, V. M., & Dubovikov, M. 1998, *ApJ*, **493**, 834
 Canuto, V. M., & Mazzitelli, I. 1991, *ApJ*, **370**, 295
 Cattaneo, F., Brummell, N. H., Toomre, J., Malagoli, A., & Hurlburt, N. E. 1991, *ApJ*, **370**, 282
 Chassaing, P., Antonia, R., Anselmetti, F., Joly, L., & Sarkar, S. 2002, *Variable Density Fluid Turbulence, Fluid Mechanics and Its Applications* (Dordrecht: Kluwer Academic Publishers)
 Christensen-Dalsgaard, J., Monteiro, M. J. P. F. G., Rempel, M., & Thompson, M. J. 2011, *MNRAS*, **414**, 1158
 Clyne, J., Mininni, P., Norton, A., & Rast, M. 2007, *NJPh*, **9**, 301
 Colella, P., & Glaz, H. M. 1985, *JCP*, **59**, 264

- Colella, P., & Woodward, P. R. 1984, JCP, **54**, 174
- Deng, L., Xiong, D. R., & Chan, K. L. 2006, *ApJ*, **643**, 426
- Deupree, R. G. 1990, *ApJ*, **357**, 175
- Deupree, R. G. 2001, *ApJ*, **552**, 268
- Dobler, W., Stix, M., & Brandenburg, A. 2006, *ApJ*, **638**, 336
- Dutton, J. A., & Fichtl, G. H. 1969, JAtS, **26**, 241
- Fryxell, B., Müller, E., & Arnett, D. 1989, in Proc. Fifth Workshop on Nuclear Astrophysics, ed. W. Hillbrandt & E. Müller (MPA-PI; Garching: MPI), 100
- Gehmeyr, M., & Winkler, K.-H. A. 1992, A&A, **253**, 92
- Gough, D. O. 1969, JAtS, **26**, 448
- Gough, D. O. 1977, *ApJ*, **214**, 196
- Grinstein, F., Margolin, L., & Rider, W. 2007, Implicit Large Eddy Simulation - Computing Turbulent Fluid Dynamics (Cambridge: Cambridge Univ. Press)
- Hanasoge, S., Duvall, T. L., & Sreenivasan, K. R. 2012, PNAS, **32**, 16
- Herwig, F. 2000, A&A, **360**, 952
- Hewitt, J. M., McKenzie, D. P., & Weiss, N. O. 1975, JFM, **68**, 721
- Hurlburt, N. E., Toomre, J., & Massaguer, J. M. 1986, *ApJ*, **311**, 563
- Hurlburt, N. E., Toomre, J., Massaguer, J. M., & Zahn, J.-P. 1994, *ApJ*, **421**, 245
- Kolmogorov, A. N. 1941, DoSSR, **31**, 538
- Kuhfuss, R. 1986, A&A, **160**, 116
- Kupka, F., & Robinson, F. J. 2007, MNRAS, **374**, 305
- Lesaffre, P., Podsiadlowski, P., & Tout, C. A. 2005, MNRAS, **356**, 131
- Li, L., Sofia, S., Ventura, P., et al. 2009, *ApJS*, **182**, 584
- Li, L. H., Ventura, P., Basu, S., Sofia, S., & Demarque, P. 2006, *ApJS*, **164**, 215
- Lighthill, M. J. 1952, RSPSA, **211**, 564
- Livescu, D., Ristorcelli, J. R., Gore, R. A., et al. 2009, JTurb, **10**, 13
- Maeder, A. 1975, A&A, **43**, 61
- Matraka, B., Wassermann, C., & Weigert, A. 1982, A&A, **107**, 283
- Meakin, C. A., & Arnett, D. 2006, *ApJL*, **637**, L53
- Meakin, C. A., & Arnett, D. 2007, *ApJ*, **667**, 448
- Meakin, C. A., & Arnett, W. D. 2010, *Ap&SS*, **328**, 221
- Nordlund, Å., Stein, R. F., & Asplund, M. 2009, LRSP, **6**, 2
- Pace, G., Castro, M., Meléndez, J., Théado, S., & do Nascimento, J.-D. 2012, A&A, **541**, 150
- Plewa, T., & Müller, E. 1999, A&A, **342**, 179
- Pope, S. B. 2000, Turbulent Flows (Cambridge: Cambridge Univ. Press)
- Porter, D. H., & Woodward, P. R. 2000, *ApJS*, **127**, 159
- Rast, M. P. 1998, JFM, **369**, 125
- Rempel, M. 2004, *ApJ*, **607**, 1046
- Renzini, A. 1987, A&A, **188**, 49
- Richardson, L. 1922, Weather Prediction by Numerical Process (Cambridge: Cambridge Univ. Press)
- Rieutord, M., & Zahn, J.-P. 1995, A&A, **296**, 127
- Rogers, T. M., & Glatzmaier, G. A. 2005, *ApJ*, **620**, 432
- Samadi, R., Belkacem, K., Dupret, M.-A., et al. 2012, A&A, **543**, 120
- Schmitt, J. H. M. M., Rosner, R., & Bohn, H. U. 1984, *ApJ*, **282**, 316
- Schroder, K.-P., Pols, O. R., & Eggleton, P. P. 1997, MNRAS, **285**, 696
- Siggia, E. D. 1994, AnRFM, **26**, 137
- Simon, G. W., & Weiss, N. O. 1991, MNRAS, **252**, 1P
- Spruit, H. 1997, MmSAI, **68**, 397
- Stein, R. F., & Nordlund, A. 1989, *ApJL*, **342**, L95
- Stellingwerf, R. F. 1982, *ApJ*, **262**, 330
- Viallet, M., Baraffe, I., & Walder, R. 2011, A&A, **531**, 86
- Viallet, M., Baraffe, I., & Walder, R. 2013, A&A, submitted
- Woodward, P., Herwig, F., Porter, D., et al. 2008, in First Stars III (AIP Conf. Proc. 990), ed. B. W. O'Shea & A. Heger (Melville, NY: AIP), 300
- Wuchterl, G., & Feuchtinger, M. U. 1998, A&A, **340**, 419
- Xiong, D.-R. 1986, A&A, **167**, 239
- Xiong, D. R., Cheng, Q. L., & Deng, L. 1997, *ApJS*, **108**, 529
- Zahn, J.-P. 1991, A&A, **252**, 179
- Zhang, C., Deng, L., Xiong, D., & Christensen-Dalsgaard, J. 2012, *ApJL*, **759**, L14